MEASUREMENTS OF THE STATIC AND DYNAMIC LOAD PERFORMANCE OF A WATER LUBRICATED HYBRID THRUST BEARING

A Thesis

by

MICHAEL S. WILKINSON

Submitted to the Office of Graduate Studies of
Texas A&M University
in partial fulfillment of the requirements for the degree of

MASTER OF SCIENCE

Chair of Committee,	Luis San Andrés
Committee Members,	Adolfo Delgado
	Theofanis Strouboulis
Head of Department,	Andreas Polycarpou

May 2019

Major Subject: Mechanical Engineering

ABSTRACT

After a successful static load testing campaign in 2015, the thrust bearing test rig has been reconfigured for dynamic load tests to determine force coefficients (stiffness, damping, and added mass). Continuous lubrication flow is supplied by a new, closed-loop water supply system capable of a wide range of operating conditions and long duration testing with little waste. In addition, a fully-instrumented loading system enables simultaneous static and dynamic (impact) loading. Cumulatively, these changes enable reliable dynamic load testing while maintaining full static load test functionality. The test rig is equipped to produce experimental results to validate bearing force coefficient model predictions.

Static force vs. displacement measurements are taken to validate test rig performance after modification to accommodate the new loading and water supply systems. Overall static load results match well with predictions as well as prior experimental results. Axial clearance (C_0) increases as the TTB lubrication pressure (P_s) increases. With a constant supply pressure (P_s), however, the test TB axial clearance (C_0) decreases as the applied axial load (W/A) increases. Large uncertainties, due in part to the allowable run out of the thrust collar (±10μm), continue to plague axial displacement measurements.

Dynamic load tests are then performed for moderate shaft speed (up to 6krpm) and quantified with force coefficients derived from the system complex dynamic stiffness function. Measurements indicate that the test thrust bearing shows no appreciable change in dynamic force coefficients (axial stiffness, damping and inertia) for the range of rotor speeds examined herein. This behavior proves the bearing behaves in a mainly

hydrostatic mode as it lacks hydrodynamic features that capitalize on bearing surface speed for performance. In contrast, with an increase in applied static load at constant supply pressure the test bearing stiffness and damping increase while added mass does not show appreciable change. Finally, an increase in supply pressure under constant applied load yields an increase in stiffness and damping coefficients with no change to added mass. As with static load measurements, inherent uncertainty associated clearance measurements are large and combine with an additional error due to repeatability of the impact tests.

A recommendation for future work is to fabricate a new rotor with tighter tolerances for the critical run out dimension. Lower run out tolerance will greatly reduce the clearance uncertainty, instilling better confidence in both static and dynamic experimental results.

DEDICATION

I thank Dr. San Andrés for the opportunity to work and learn at the Turbomachinery Laboratory. Additionally, I thank the Turbomachinery Research Consortium for their financial support. I thank Mr. Michael Rohmer, Mr. Hardik Jani, Mr. Hameed Haq, Mr. Giovanni Palini, Mr. Travis Cable, Ms. Avery Carnahan, Ms. Casey Yowell, Mr. Blake Bontz, Mr. Juan Francisco Ordonez and other colleagues at the Turbomachinery Laboratory for their support. Finally, thanks to my family for their encouragement.

CONTRIBUTORS AND FUNDING SOURCES

This work was supervised by a thesis (or) dissertation committee consisting of Professor(s) San Andrés [advisor] and Delgado of the Department of Mechanical Engineering and Professor Strouboulis of the Department of Aerospace Engineering. All work for the thesis (or) dissertation was completed by the student, under the advisement of Professor San Andrés of the Department of Mechanical Engineering.

This work was made possible in part by funding from the Turbomachinery Research Consortium, and the Turbomachinery Laboratory at Texas A&M University.

NOMENCLATURE

1-DOF	One degree of freedom
A	Thrust bearing area [m^2]
C_0	Axial clearance between thrust bearing center and thrust collar [μm]
C_{TTB}	Thrust bearing damping coefficient [Ns/m]
F_{Cable}	Force exerted by taut cable [N]
F_d	Applied dynamic (impact) load [N]
FFT	Fast Fourier Transform
F_{TTB}	Thrust bearing reaction force [N]
H	Dynamic (complex) stiffness of thrust bearing $= H_R + i\, H_I$
HTB	Hybrid Thrust Bearing (hydrostatic plus hydrodynamic)
i	Imaginary unit, $i=\sqrt{-1}$
K_{Cable}	Taut cable stiffness [N/m] = *93.15 kN/m*
K_{TTB}	Thrust bearing stiffness coefficient [N/m]
M	Mass of thrust bearing, load shaft and load cell [kg]
M_{TTB}	Thrust bearing added mass coefficient [Ns^2/m]
N	Number of impacts for average
P_J	Journal bearing supply pressure [bar(g)]
P_T	Thrust bearing supply pressure [bar(g)]
R_{out}	Thrust collar outer radius [cm]

SSV	Subsynchronous speed vibration
TTB	Test Thrust Bearing
VI	Visual Interface
VFD	Variable Frequency Drive
z	Relative displacement between rotor and test thrust bearing [μm]
z_R	Absolute axial displacement of rotor [μm]
z_{TTB}	Absolute displacement of test thrust bearing [μm]
Ω	Rotor speed [rad/s]
ω	Excitation frequency [rad/s]
W/A	Specific Load [bar]

TABLE OF CONTENTS

Page

ABSTRACT ii

DEDICATION iv

CONTRIBUTORS AND FUNDING SOURCES v

NOMENCLATURE vi

TABLE OF CONTENTS viii

LIST OF TABLES x

LIST OF FIGURES xi

INTRODUCTION 1

TEST RIG DESCRIPTION 2

LITERATURE REVIEW 8
  Background 8
  Principle of Operation of a Hybrid Bearing 8
  High Performance Thrust Bearings for High Rotor Speed Applications 9
  Parameter Identification Methods 10
  Previous Work 11

TEST RIG MODIFICATIONS 16
  Water Supply System 16
  Dynamic Load Mechanism 19

SYSTEM MODEL FOR PARAMETER IDENTIFICATION 28

DATA ACQUISITION AND PROCESSING 32
  Data Acquisition 32
  Data Processing 33

THRUST BEARING PERFORMANCE 36

STATIC LOAD PERFORMANCE 37
  Static Load Tests at Various Supply Pressures and Rotor Speeds 38
  Static Load Tests at Various Rotor Speeds 41

DYNAMIC LOAD PERFORMANCE 45
  Dynamic Load Tests at Various Supply Pressures and a Fixed Rotor Speed 46
  Dynamic Load Tests at Various Rotor Speeds and a Fixed Supply Pressure 50

CONCLUSION 54

REFERENCES 56

APPENDIX A INSTRUMENTATION 59

APPENDIX B ROTOR THRUST COLLAR PLANE EQUATION DERIVATION 60

APPENDIX C UNCERTAINTY ANALYSIS 63
  Static Load Measurements 63
  Dynamic Load Measurements 64

APPENDIX D DETERMINATION OF CABLE STIFFNESS 66

LIST OF TABLES

Page

Table 1. Test Matrix for static load tests at null to moderate shaft speed. 38

Table 2. Test Matrix for dynamic load tests for operation at various TTB supply pressure and applied static load conditions. 45

Table 3. Test Matrix for dynamic load tests for operation at null to moderate shaft speeds. 46

Table 4. Instrumentation utilized for TTB dynamic load testing 59

Table 5. Horizontal and vertical positions of each eddy current sensor relative to the center of the thrust bearing. 61

LIST OF FIGURES

Page

Figure 1. Photograph of test rig (2015) 4

Figure 2. Cross sectional view of the thrust bearing test rig [1]. 5

Figure 3. Photograph [4] and physical parameters of hybrid (hydrostatic/ hydrodynamic) thrust bearing 5

Figure 4. Photograph of rotor [15] 6

Figure 5. Schematic view of the flexure pivot, tilting pad hydrostatic journal bearing. [3] 6

Figure 6. Schematic View of Test Rig: Thrust and Journal Bearings Represented as Mechanical Elements with Stiffness and Damping Coefficients [4] 7

Figure 7. Schematic view of closed loop water supply system for thrust bearing test rig. 18

Figure 8. Photograph depicting major components of the water supply system. 19

Figure 9. Schematic diagram of an early axial loading mechanism. 21

Figure 10. Impact load test to determine resonant frequency of a strain gauge load cell. 23

Figure 11. Dynamic signal analyzer output of strain gauge load cell impact test showing a resonant frequency at 1728 Hz with good coherence between the delivered impact load (input) and the measured acceleration (output). 22

Figure 12. Schematic of redesigned, cable-loaded loading system and the geometry of the taut cable used to derive the equivalent static load along the axial direction, Fr. 25

Figure 13. Photograph of taut cable load mechanism. 26

Figure 14. Photograph of the updated impact tip/load cell assembly. The dynamic load cell utilizes a threaded connection to both the impact tip and the load shaft. Preload is set by tensioning these threaded connections, enabling the dynamic load cell to measure both compressive and tensile forces. 27

Figure 15. Axial acceleration measurements on TTB housing due to an impact load (a) with early configuration of load mechanism, and (b) with new configuration with taut cable. 27

Figure 16. Schematic view of 1-DOF model of test TB for parameter identification. 29

Figure 17. Visual Interface (VI) front panel recording dynamic impact test data. 33

Figure 18. Sample linear curve fit of the (a) real and (b) imaginary portions of the TTB complex stiffness (H) vs frequency. W/A is the specific load defined as the axial load per unit area. Note that A = 32.6 cm^2 35

Figure 19. Axial clearance (C0) versus specific load (W/A) for operation at four TTB supply pressures (Ps) and rotor speed at 3 krpm. Horizontal error bars represent the uncertainty in the axial load at a 95% confidence interval. Vertical error bars indicate the uncertainty in the axial clearance due to the machined runout of the rotor 35

Figure 20. Axial clearance (C0) versus specific load (W/A) for operation at four TTB supply pressures (Ps) and rotor speed at 4 krpm. Horizontal error bars represent the uncertainty in the axial load at a 95% confidence interval. Vertical error bars indicate the uncertainty in the axial clearance due to the machined runout of the rotor. 40

Figure 21. Axial clearance (C0) versus specific load (W/A) for operation at four TTB supply pressures (Ps) and rotor speed at 5 krpm. Horizontal error bars represent the uncertainty in the axial load at a 95% confidence interval. Vertical error bars indicate the uncertainty in the axial clearance due to the machined runout of the rotor. 40

Figure 22. Axial clearance (C0) versus specific load (W/A) for operation at four TTB supply pressures (Ps) and rotor speed at 6 krpm. Horizontal error bars represent the uncertainty in the axial load at a 95% confidence interval. Vertical error bars indicate the uncertainty in the axial clearance due to the machined runout of the rotor. 35

Figure 23. Axial clearance (C0) versus specific load (W/A) for operation at various rotor speeds for operation with supply pressure Ps = 2.76 bar(g). Horizontal error bars represent the uncertainty in the axial load at a 95% confidence interval. Vertical error bars indicate the uncertainty in the axial clearance due to the machined runout of the rotor. 42

Figure 24. Axial clearance (C0) versus specific load (W/A) for operation at various rotor speeds for operation with supply pressure PS = 3.45 bar(g). Horizontal error bars represent the uncertainty in the axial load at a 95% confidence interval. Vertical error bars indicate the uncertainty in the axial clearance due to the machined runout of the rotor. 42

Figure 25. Axial clearance (C0) versus specific load (W/A) for operation at various rotor speeds for operation with supply pressure PS = 4.14 bar(g). Horizontal error bars represent the uncertainty in the axial load at a 95% confidence interval. Vertical error bars indicate the uncertainty in the axial clearance due to the machined runout of the rotor. 43

Figure 26. Axial clearance (C0) versus specific load (W/A) for operation at various rotor speeds for operation with supply pressure PS = 4.83 bar(g). Horizontal error bars represent the uncertainty in the axial load at a 95% confidence interval. Vertical error bars indicate the uncertainty in the axial clearance due to the machined runout of the rotor. 43

Figure 27. Experimentally measured and predicted axial stiffness coefficient (Kz) for TTB operating with water supplied at 2.75, 3.45 and 4.14 bar(g) and shaft speed of 3 krpm. Applied specific axial load, W/A = 0.49 bar, 0.61 bar, and 0.73 bar. 48

Figure 28. Measured and predicted damping coefficient (Cz) for TTB operating with water supplied at 2.75, 3.45 and 4.14 bar and shaft speed of 3 krpm. Applied specific axial load, W/A = 0.49 bar, 0.61 bar, and 0.73 bar. 49

Figure 29. Measured and predicted added mass coefficient (Mz) for TTB operating with water supplied at 2.75, 3.44 and 4.13 bar and shaft rotational speed of 3 krpm. Applied specific axial loads of 0.49 bar, 0.61 bar, and 0.73 bar. 50

Figure 30. Measured and predicted stiffness (Kz) for the TTB operating with water supplied 4.83 bar and shaft speed of 3 krpm, 4krpm, 5krpm and 6krpm. Specific axial load W/A = 0.49 bar, 0.61 bar, and 0.73 bar is applied to the TTB. 51

Figure 31. Measured and predicted damping (Cz) for the TTB operating with water supplied at 4.83 bar psi(g) and shaft speed of 3 krpm, 4krpm, 5krpm and 6krpm. Specific axial load W/A = 0.49 bar, 0.61 bar, and 0.73 bar is applied to the TTB. 52

Figure 32. Measured and predicted added mass (Mz) for the TTB operating with water supplied at 4.83 bar psi(g) and shaft speed of 3 krpm, 4krpm, 5krpm and 6krpm. Specific axial load W/A = 0.49 bar, 0.61 bar, and 0.73 bar is applied to the TTB. 53

Figure 33: Reference diagram of a thrust bearing for geometric calculation of clearance as a function of displacements recorded at T1, T2, and T3 60

Figure 34. Averaged displacement response for four series of 25 impacts performed for operation at a rotor speed of 3krpm, thrust bearing supply pressure of 3.45 bar(g) 65

Figure 35. Schematic of an ad-hoc setup used to record the axial stiffness of a static loading mechanism. 67

Figure 36. Applied force vs. displacement results for determination of the axial stiffness of the static loading mechanism. 67

INTRODUCTION

In rotating machinery, fluid lubricated thrust bearings maintain axial position and support axial loads applied to the rotor. The performance and reliability of these machines depend on adequate axial load support tailored to the operating conditions of the machine. Prediction of these thrust forces is largely empirical, emphasizing the need to design and test thrust bearings for use in reliable rotating equipment [1].

Presently, dynamic load tests are performed with a purpose-built test rig on a hybrid thrust bearing. The thesis results will advance bearing technology by offering experimental data to compare with predictions generated by a predictive software in Ref. [2].

In 2015, a water lubricated thrust bearing test rig is revamped after severe damage was incurred in 2013 due to large amplitude vibrations during operation with air lubricated radial bearings [1]. Static load tests performed in 2015 [3] paved the way for the dynamic load testing discussed herein.

This thesis reviews relevant literature pertaining to the project, describes test rig modifications, overviews system modelling, outlines the data acquisition and processing methods, and presents test results for dynamic impact load tests. The test rig is presently used to measure the static and dynamic performance for various thrust bearing and face seals.

TEST RIG DESCRIPTION

Figure 1 shows a photograph and Figure 2 shows a cross section view [4] of an existing thrust bearing test rig constructed to quantify the static and dynamic load performance of water lubricated hybrid thrust bearings. Water supplies two flexure-pivot tilting-pad hydrostatic journal bearings to enable the lateral support of the rotor. Two water-lubricated hybrid (hydrostatic and hydrodynamic) thrust bearings, test and slave, control the axial position of the rotor.

Figure 3 depicts a photograph of the test hybrid (hydrostatic plus hydrodynamic) thrust bearing (HTB) [4]. With sufficiently small clearances between the HTB and the rotor thrust collar (see Figure 4), load support is generated by restricting water flow through eight orifices to pressurize the eight corresponding recessed areas. An identical, albeit with slightly larger orifices, smaller pockets and split in half for ease of installation, slave thrust bearing counteracts the load generated by the test thrust bearing. Both HTBs are manufactured with 660 Bearing Bronze and have inner and outer diameters of 40.6 mm and 76.2 mm, respectively. Each pocket is 20° in arc length, 8.13 mm in radial length, pocket depths of 0.51 mm (Test) and 0.44 mm (Slave).

Figure 5 shows one of two identical flexure pivot, tilting pad hybrid (hydrostatic/hydrodynamic) radial bearings supporting the rotor [3]. Electron discharge machining (EDM) is used to manufacture the flexible pivot, tilting pad bearing out of a 660 Bearing Bronze material. The bearings are fabricated in two pieces, top and bottom halves, to simplify the installation process. Both the inner diameter and the bearing length are manufactured to be 3.81 cm for an operating radial clearance of 89 μm. Both bearings have four 72° pads, 20% preload, with 60% pivot offset [5]. The 8.7 lb stainless steel rotor, shown in Figure 4, has its center of mass midway between two radial bearings. The rotor consists of opposing test and slave thrust collars and a threaded connection to interface with the flexible motor coupling.

A loading mechanism moves the test thrust bearing axially and applies the load to the rotor thrust collar. As shown on the left of Figure 2, two air bearings support the non-rotating load shaft while allowing the shaft to move axially with minimal friction when a load is applied. The rotor transmits the load to the slave thrust bearing. The slave bearing side of the rotor connects to a Variable Frequency Drive (VFD) controlled electric motor via a flexible coupling.

Figure 6 shows a schematic view of the test rig with the thrust bearings and journal bearings represented as mechanical elements with stiffness and damping characteristics (radial and axial) [4]. In the system modelling section of this report, the assembly is represented as a one degree of freedom system for determination of the axial bearing force coefficients (stiffness, damping, and added mass).

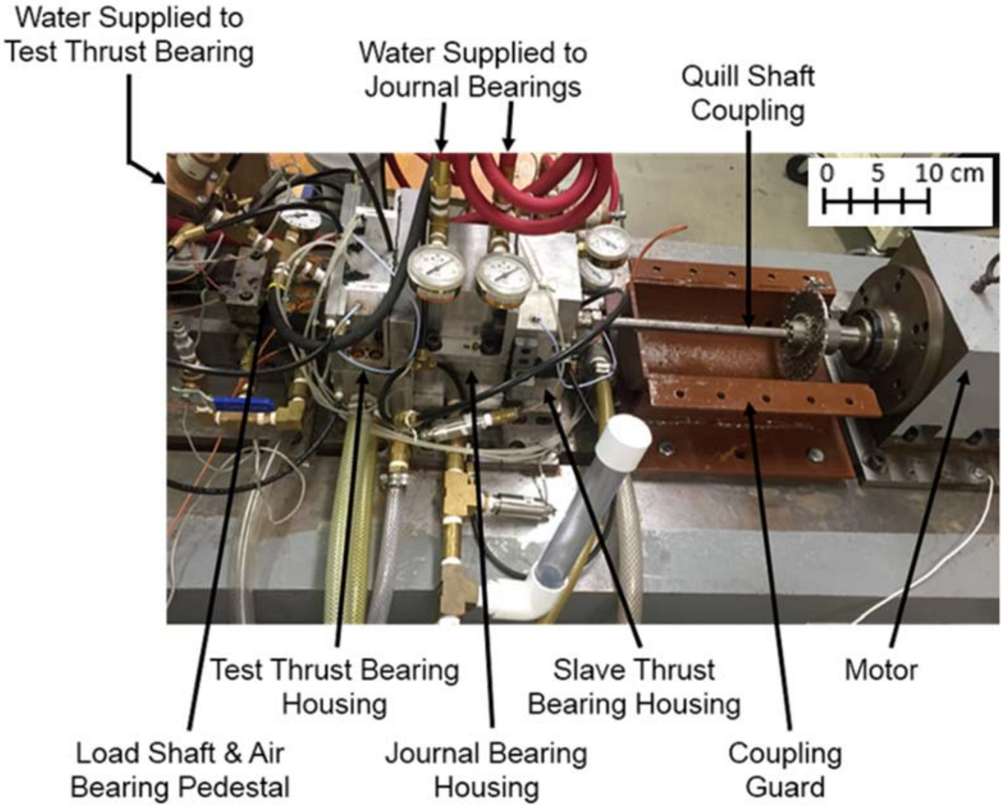

Figure 1. Photograph of test rig (2015)

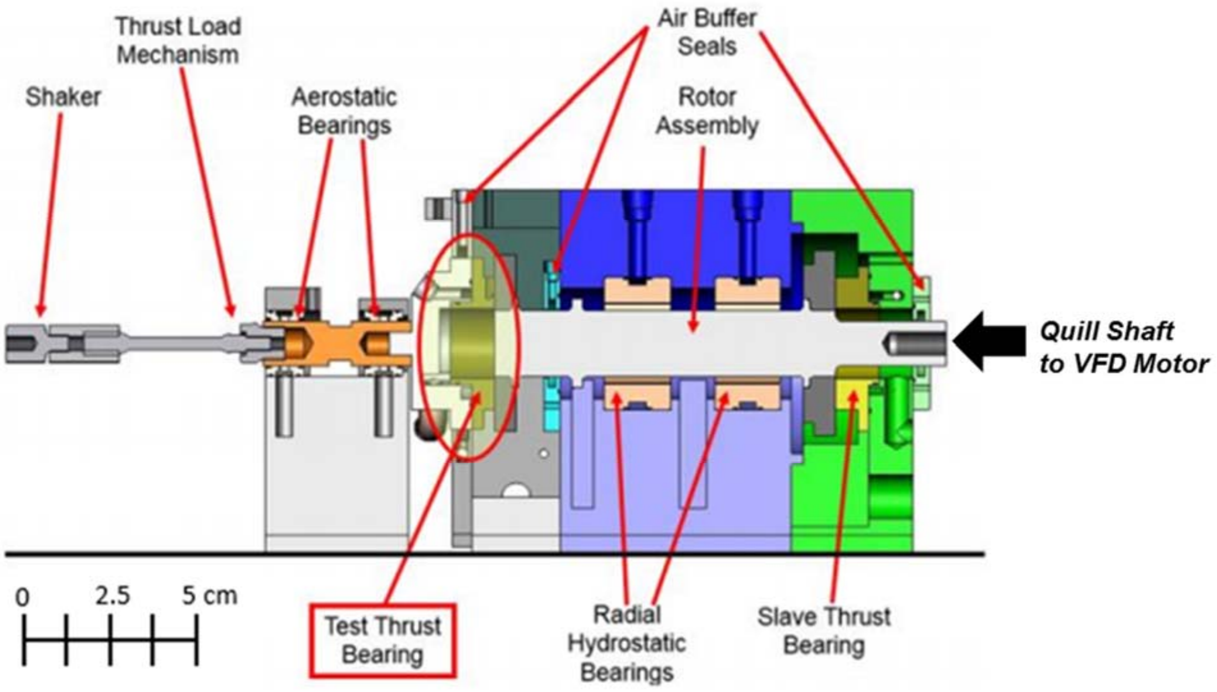

Figure 2. Cross sectional view of the thrust bearing test rig [1].

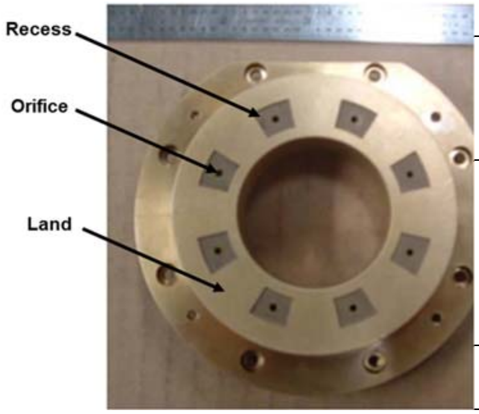

	Material: 660 Bearing Bronze	Slave Bearing	Test Bearin
Thrust Face	Inner Diameter, D_{in}	40.64 mm	
	Outer Diameter, D_{out}	76.2 mm	
	Thrust Bearing Area, A	32.6 cm^2	
	Flange Outer Diameter	98.43 mm	
Pocket	Number of Pockets	8	
	Arc Length	20°	
	Radial Length	8.13 mm	
	Depth	0.44 mm	0.51 mm
	Pocket/Wetted Area Ratio	0.19	
Orifice	Orifices/Pocket	1	
	Diameter, d_{orif}	1.80 mm	1.55 mm

Figure 3. Photograph [4] and physical parameters of hybrid (hydrostatic/hydrodynamic) thrust bearing

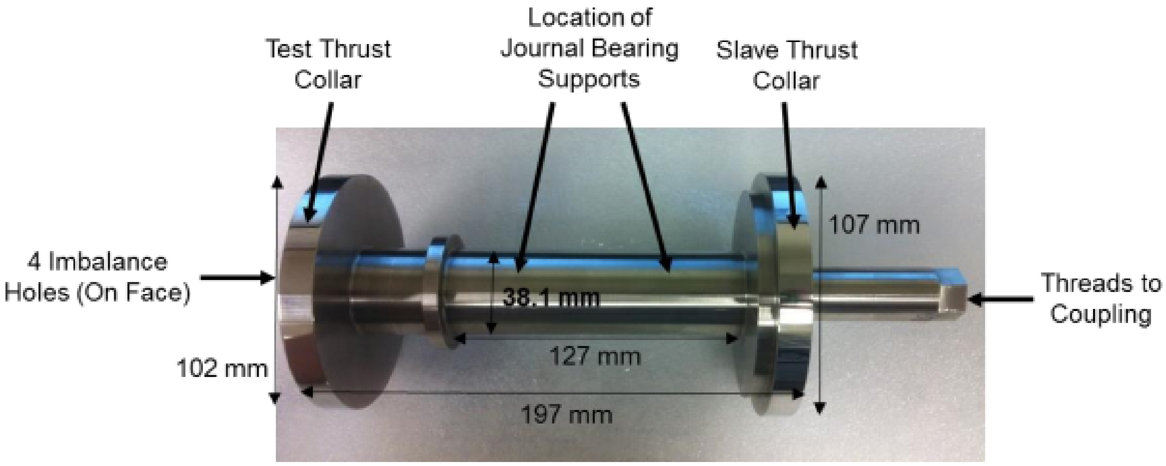

Figure 4. Photograph of rotor [15]

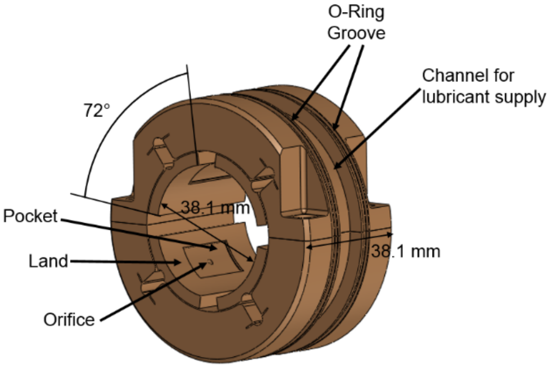

Figure 5. Schematic view of the flexure pivot, tilting pad hydrostatic journal bearing. [3]

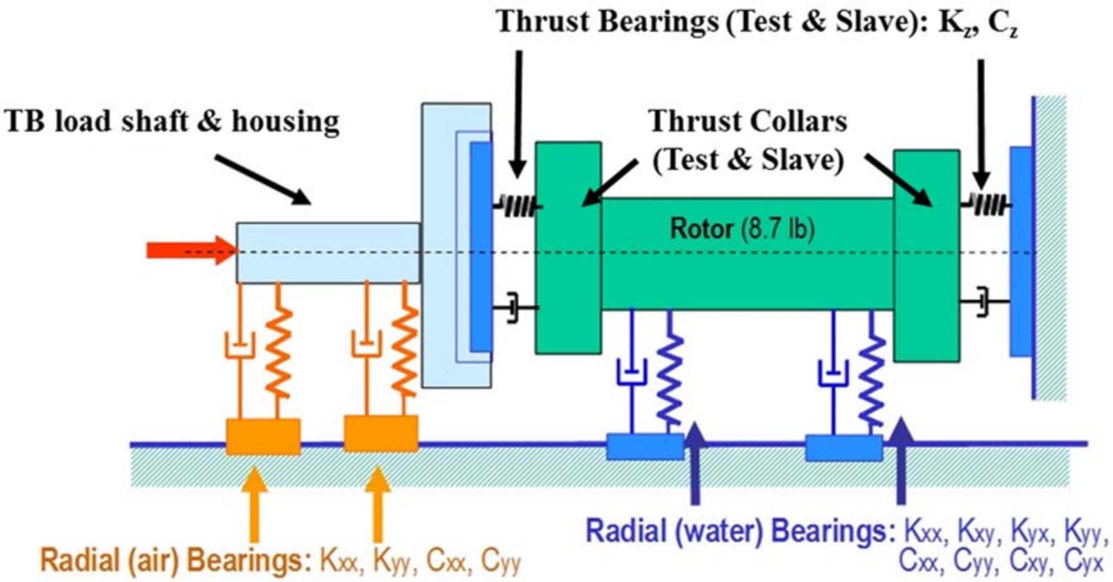

Figure 6. Schematic view of test rig: thrust and journal bearings represented as mechanical elements with stiffness and damping coefficients [4]

LITERATURE REVIEW

Background

Hybrid Thrust Bearings (HTBs) exhibit features of both hydrostatic and hydrodynamic bearings. Where hydrodynamic bearings function with a fluid film pressure generated from a rotating shaft, hydrostatic bearings provide support without shaft speed by utilizing an external pressurization system. This ensures no contact of surfaces at a low or null rotational speed though at the cost of external energy required to pressurize the bearing. Lubricant supply pressure and shaft rotational speed dictate the bearing load capacity, drag torque, and axial force coefficients.

Principle of Operation of a Hybrid Bearing

Rowe (1983) [6] details HTB operation with its load support and stiffness generated as fluid flow passes through a flow restrictor (such as an orifice, a capillary or a constant flow valve). An additional flow resistance occurs as the fluid flows through a small clearance or film land region. As this clearance decreases, the flow rate reduces and the head loss through the orifice also decreases; causing an increase in recess pressure. The recess pressure does not exceed supply pressure except for cases where shaft speed is large enough to generate an additional hydrodynamic pressure. Hybrid bearings perform like hydrostatic bearings at a low rotational shaft speed and exhibit hydrodynamic behavior with a significantly high shaft speed. An increased recess pressure induces a higher load on the rotor and increases the gap (clearance) between the rotor and the bearing. The opposite is true for a decrease in applied load; flow rate and head loss through the orifice increase, thus causing the recess pressure to decrease. A decrease in recess pressure with a constant applied load induces a smaller clearance between the rotor and the bearing. Bearing stiffness and damping force coefficients are thus related to the conditions of the supply flow.

High Performance Thrust Bearings for High Rotor Speed Applications

In cryogenic fluid turbo pump applications fluid film hybrid bearings offer an alternative to ultra-precision ceramic ball bearings for rotor support [7]. High shaft speeds utilized by turbo pumps mandate the use of bearings with little or no surface speed limitation, a feature unique to fluid film hybrid bearings. These bearings allow the turbopump to be smaller and lighter while operating with an increased mechanical efficiency.

Using a bulk flow analysis, San Andrés (2000) [8] predicts the performance of a multi-recess, orifice-compensated, angle injected HTB. For a high pressure cryogenic density turbo pump example, the study analyzes bearing operation with high shaft speed (180 krpm) and a high pressure differential (550 bar). The bearing stiffness coefficient is highest when the recess pressure is 60% of the supply pressure (both relative to ambient conditions). The bearing damping coefficient increases with a decrease in clearance and an increase in rotor speed. Centrifugal fluid inertia becomes an issue at a sufficiently high rotor speed and a low load conditions as it may induce starvation on the bearing inner side diameter and a suction pressure just downstream of the recess. Including the effect of fluid inertia across the recesses and the film lands, the damping coefficient is higher and the stiffness coefficient lower than the analysis considering the recesses alone, indicating that fluid inertia plays a large role in fluid bearing performance.

Safar (1983) [9] analyzes the effect of centrifugal forces on misaligned hydrostatic thrust bearings. Centrifugal forces cause load capacity and drag torque to reduce considerably while increasing the flow rate across the bearing. Centrifugal effects diminish with an increase in collar angular misalignment.

San Andrés (2002) [2] utilizes his computational model to study the effects of angular misalignment on HTB performance for a cryogenic turbopump operating at a rotational speed of 180 krpm. Axial and moment-angle stiffness coefficients (both static and dynamic) peak when the recess pressure ratio is approximately 0.6. Axial damping, direct moment angle damping and cross-coupled moment angle stiffness coefficients increase moderately with load for high clearance/low load conditions and then rapidly with load for low clearance/high load conditions due to the increased hydrodynamic effect while operating at a low clearance. With an increase in misalignment angle between the thrust bearing and the rotor, the moment angle and axial stiffness coefficients increase while axial force and drag torque remain unaffected. Additionally, an increase in misalignment angle causes an increased differential in pressure across the recesses and film lands which, in turn, causes a decrease in the mass flow rate through the inner diameter of the bearing.

Parameter Identification Methods

Parameter identification requires measurement of the rotor displacement (response) due to a controlled external load excitation [10]. These measurements allow the estimation of the bearing complex stiffness (or impedance) in the frequency domain [11]. Periodic force and impact load excitations applied to the thrust bearing are the most feasible means to excite the system. Periodic loads can be exerted through a shaker attached to the test bearing. Independent adjustment of the shaker frequency allows studying frequency dependence of the bearing force coefficients [10]. Alternatively, a transient load excitation of a rotor-bearing system through impact loads has the advantage of exciting a broad range of excitation frequencies in a single experiment, thus reducing the time required for testing.

Previous Work

Prior to the current work, former students of Texas A&M University constructed and performed tests with the above described test rig.

Forsberg (2008) [12] designs and constructs a (non-rotating shaft) thrust bearing test rig to measure the performance of a water-lubricated, eight pocket HTB operating with supply pressure ranging from 3.45 bar(g) to 17.24 bar (g). The pocket pressure ratio (ratio of pocket pressure to supply pressure to the test thrust bearing, $P_{Ratio}=P_{pocket}/P_{supply}$) has a large influence on the operating clearance (load) between the thrust bearing and thrust collar of the rotor. An increase in pocket pressure, stemming from either an increase in supply pressure or a decrease in clearance, correlates to an increase in bearing load capacity and stiffness. Measurements of flow and load capacity agree within 20% of predictions generated by San Andrés [2], while a static stiffness approximation demonstrates a large discrepancy from predictions due to misalignment between the thrust bearing face and the thrust collar of the rotor.

Ramirez (2008) [13] continues Forsberg work with the same water lubricated, 8 pocket HTB with supply pressure ranging from 3.45 bar (g) to 17.24 bar (g) but with an operating shaft speed ranging from 7.5 krpm to 17.5 krpm (ΩR = 69.8/m/s). Shaft speed is found to have little influence on the load capacity and axial stiffness of the test bearing. At a high shaft speed and low load, flow rate measurements through the inner diameter indicate the onset of fluid starvation due to centrifugal fluid flow acceleration. Inlet flow rate, inner diameter discharge flow rate, load capacity, and recess pressure ratio measurements agree closely with predictions derived in [2], differing by 1%, 5%, 7%, and 10%, respectively.

Esser (2010) [14] carries on work by Forsberg and Ramirez by determining the effect of orifice diameter (1.67 mm, 1.80 mm, and 1.93 mm) on the performance of the same water-lubricated, eight pocket HTB with supply pressure ranging from 3.45 bar (g) to 17.24 bar (g) and shaft speeds ranging from 7.5 krpm to 17.5 krpm. With a constant applied load and a constant thrust bearing supply pressure, the bearing stiffness and clearance increase with an increase in feed orifice diameter. Flow rate increases with a larger orifice diameter, preventing the onset of inner bearing starvation predicted by Forsberg and Ramirez [12, 13]. A limited increase in bearing axial stiffness occurs when the orifice diameter changes from 1.80 mm to 1.93 mm, while the flow rate demanded is significantly higher. Measurements for inlet flow rate, inner diameter discharge flow rate, recess pressure, clearance, and axial stiffness coefficient agree well with predictions.

San Andrés et al. (2016) [4] examine the performance of a hydrostatic thrust bearing subjected to increasing static load (max. 3600 N), shaft speed up to 17.5krpm (ΩR = 70 m/s) and increasing supply pressure (max. 17.2 bar). Predictions generated from a bulk flow model [2], accounting for fluid inertia and turbulent flow effects, agree well with the experimental results. Measured parameters include flow rates (supply and return through thrust bearing inner diameter), pocket pressure, and fluid film clearance. As the applied load increases, predictions and measurements show that the film clearance and flow rate decrease exponentially. Measurements validate a predicted fluid starvation event at the highest speed and lowest supply pressure condition. Measured flow rate and bearing pocket pressure data enable the empirical estimation of the bearing discharge coefficient for use in the predictive tool.

Rohmer (2016) [15] details a catastrophic failure (occurring in 2013) as well as many repairs and modifications to the test rig described above. In 2014, the test rig was modified to host hydrostatic gas (air) bearings. The failure occurred when a high amplitude subsynchronous speed vibration (SSV) was observed at approximately 28 krpm [1]. After the failure incident, the test rig was converted back to operation with water. Revamping of the test rig, completed in 2015, includes: manufacturing two new rotors, repairing the damaged threads on the housing, aligning the motor shaft centerline and the test rotor centerline, upgrading the water manifold to mitigate pressure losses, designing a load system capable of static and/or dynamic loads, installing instrumentation, and developing means of data acquisition. Measurements of the free-free mode natural frequencies and mode shapes of the rotor-coupling system show that the test rotor and quill shaft coupling must be considered as a single unit for accurate rotordynamic analysis.

Without rotor speed, Rohmer et al. (2018) [3] measure the static load performance of a hybrid thrust bearing lubricated with water at room temperature (24 °C), increasing supply pressure (max. 4.14 bar(g)), and shaft speed up to 3 krpm. The axial clearance increases as the water supply pressure increases for a constant load. At a constant water supply pressure, the axial clearance decreases as the axial load increases. As the axial clearance decreases, the flow rate also decreases which leads to a higher flow resistance across the film lands and a higher recess pressure. Static stiffness is derived based on the change in axial clearance with various applied static loads.

In summary, static load performance is available [3] for an 8-pocket HTB, water lubricated and rotor speed up to 3 krpm (12 m/s max surface speed). Experimental results from static load tests qualitatively match with predictions. Angular misalignment between the TTB and the rotor thrust collar obscures the test data, causing large uncertainties in clearance measurements between the TTB and rotor thrust collar. Although misalignment can be quantified, it cannot be eradicated without extensive modifications to the test rig.

Moving forward, dynamic load tests are needed to quantify the HTB force parameters (stiffness, damping, and added mass). Because many impact tests must be performed during each test condition, thus equating to a longer test duration compared to that in static load tests, the test rig must be modified for a more efficient supply of lubricant flow. A new loading mechanism is also required to apply both static and dynamic loading simultaneously. Finally, a comparison of the test extracted bearing force coefficients with predictions will validate the predictive software, providing a valuable tool for the design of machinery utilizing these bearings.

TEST RIG MODIFICATIONS

Heretofore, the aforementioned test rig was used exclusively for static load tests. Because static load tests are inherently short-duration, the efficiency of the bearing lubrication system was not a limiting factor. The previous test rig configuration did not recycle the exhausted lubrication fluid, resulting in a large amount of wasted water. Impact tests involve the averaging of many individual experiments for each test condition. Thus, to maintain consistency in the operating conditions, the lubrication supply system must be maintained for the duration of each series of tests. In addition, to conserve water, a new closed-loop system is implemented to accommodate the longer duration testing.

Water Supply System

Impact load testing involves the averaging of many individual load impact tests for every test condition, a significantly more time consuming procedure than static load testing. This long duration impact testing and the desire to achieve higher bearing supply pressure drove the construction of a continuous water supply system. Prior operation [16] sourced water from the test facility central water system and discarded it after passing through the test rig. The replacement system recycles fluid returning from the test rig and is capable of achieving a maximum pressure of 222 psig at 25 GPM, a significant improvement over the prior system.

Figure 7 shows a schematic of the water supply system for the thrust bearing test rig which consists of a reservoir tank, main pump, return pump, heat exchanger, and various valves and instrumentation components [17]. Figure 8 shows a picture of the major components of the water supply system prior to assembly. A vertical 17 stage centrifugal pump and 7 HP electric motor make up the main pump system operating at constant speed (1450 rpm). Deionized water is supplied to the pump directly from a 500-gallon reservoir tank while flow to the test rig is controlled by a downstream globe valve that directs a portion of the flow back to the tank. A 2 HP, self-priming centrifugal pump re-charges fluid passing through the test rig through an air-cooled heat exchanger and back to the tank. Apart from the tank, all system components are housed in a freestanding pump shed located just outside of the facility and linked to the test rig through a series of PVC and steel piping. A deionization plant supplies deionized water to the tank for initial fill-up and to replace fluid lost through leakage at the test rig. Deionized water is beneficial for water-lubricated systems as it mitigates the effects of corrosion on the bearing metal surfaces and various system components decreasing down time and cost associated with cleaning and replacing components. A pump shed (located outside of the test-cell) houses system components for protection from the environment.

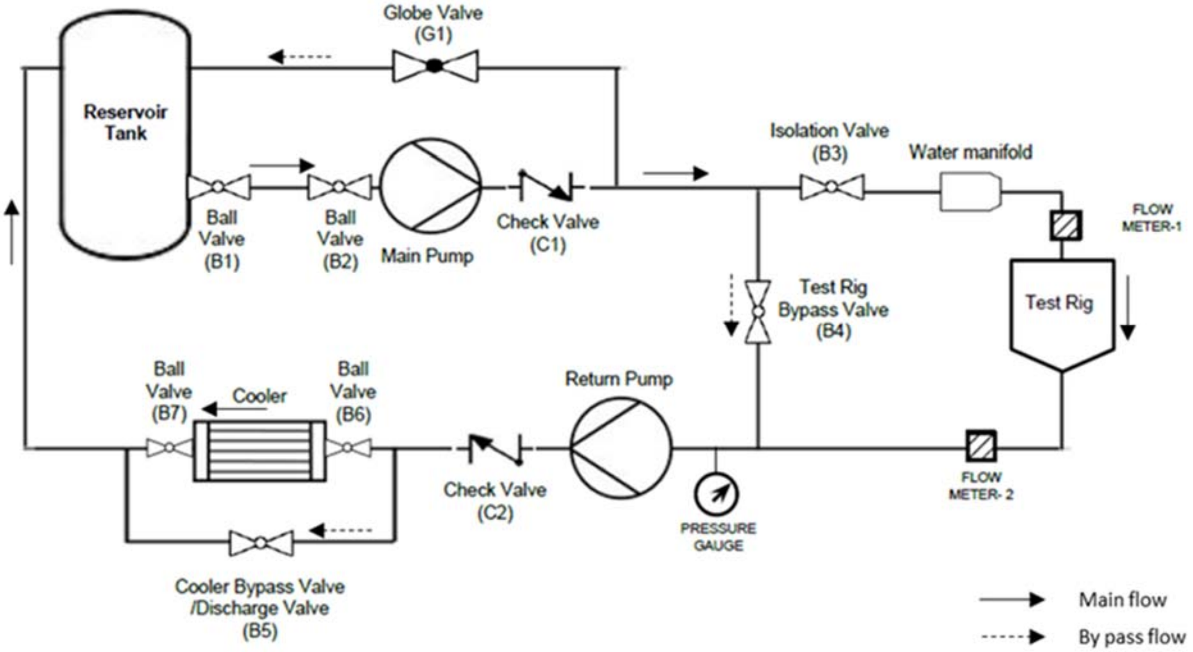

Figure 7. Schematic view of closed loop water supply system for thrust bearing test rig.

Figure 8. Photograph depicting major components of the water supply system.

Dynamic Load Mechanism

To determine the method of excitation necessary for dynamic performance testing, two methods are considered: impact loads and shaker load testing. Impact load tests involve the application of a short duration force which excites a broad band of frequencies in a system. Impact load testing requires averaging of many individual tests to reduce the amount of noise interference from the measurements. Shaker load testing involves use of an approximately sized electromagnetic shaker which applies a force at a prescribed frequency. Ultimately, impact load testing is utilized due space constraints and availability of equipment. Note also that, the test rig is fixed to a rigid, solid table, and installation and alignment of a shaker to apply dynamic loading along the axial direction was not practical.

Prior to 2015, loads applied to the test thrust bearing were exclusively static. The application and subsequent measurement of dynamic loads required the loader to be redesigned to achieve an effective superposition of a transient force to a static load both exerted along the axial direction. Figure 9 shows a schematic of an early version of the loading mechanism which utilizes a lever to apply a static load from a spring in tension and dynamic load through an impact load to the base. A load cell located on the tip of an impact hammer records the impulse load while a strain gauge load cell mounted in series with the loader and the load shaft measures the static load applied by the spring/lever system. A spherical coupling between the load cell and load shaft is used to reduce the moment applied to the load shaft. This design proved to be effective for application of a static load but ineffective for dynamic loading (with impact loads).

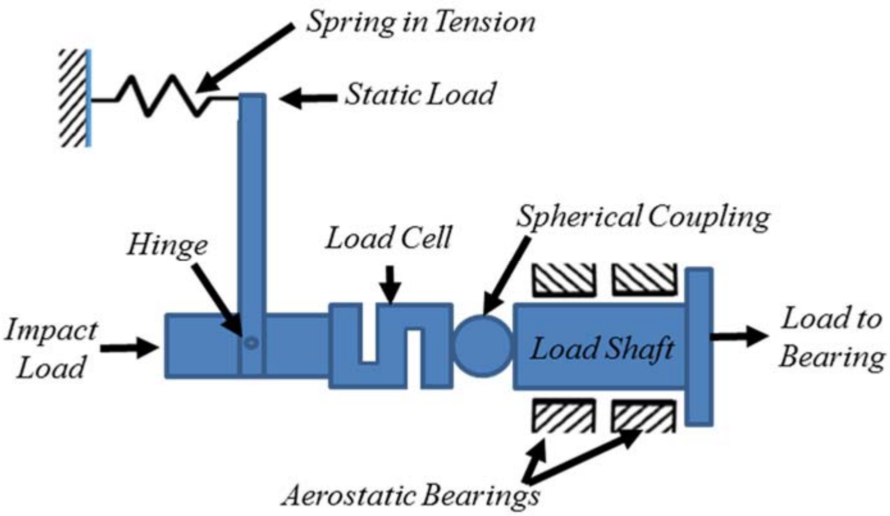

Figure 9. Schematic diagram of an early axial loading mechanism.

Deficiencies in the previous version of the loading mechanism (for dynamic loading) are attributed to three primary sources. First, a significant component of the applied impact load has a perpendicular component to the axial direction. Only a portion of the applied load is transmitted axially to the test thrust bearing, despite the use of the spherical coupling. Loads applied with the lever system did not translate as expected to the strain gauge load cell, indicating that only a portion of the applied load is transmitted to the TTB axial direction. Upon further investigation, rub marks on the aerostatic bearing surfaces indicate loading perpendicular to the axial direction. Additionally, a resonance (approximately 1,728 Hz) of the strain gauge load cell subjected to impact loading affected the measurement of the test thrust bearing response. Due to the inherently small amplitude motion of the thrust bearing under typical test conditions, structural vibration of the loading mechanism must be minimized.

The strain gauge load cell, used to measure static load, is removed from the system and suspended with a cable as shown in Figure 10. A simple impact load test identifies the natural frequency of the strain gauge load cell in the axial direction. An impact hammer applies a dynamic load to the load cell while an accelerometer records the vibration, all in the axial direction. Figure 11 shows the structural resonant frequency of the strain gauge load cell occurs at approximately 1,728 Hz, as measured by a dynamic signal analyzer. Although the frequency of the structural load cell vibration is higher than that of the TTB, the vibration amplitude is larger than the axial response of the bearing which distorts the frequency response of the system. Ultimately, the strain gauge load cell is removed from the load shaft assembly in favor of a much smaller dynamic load cell which is better-suited suited for the sampling frequency required for the dynamic load tests.

Furthermore, the dynamic load measured by the impact gun load cell (mounted to the tip of the gun) captured only the initial compressive impact load but failed to register the test thrust bearing forced response, both tensile and compressive. This realization influenced the move to an integral load cell configuration where the load cell is rigidly connected as part of the moving load mechanism, as shown in Figure 14. By preloading the load cell during the assembly process, both tensile and compressive load measurements are possible.

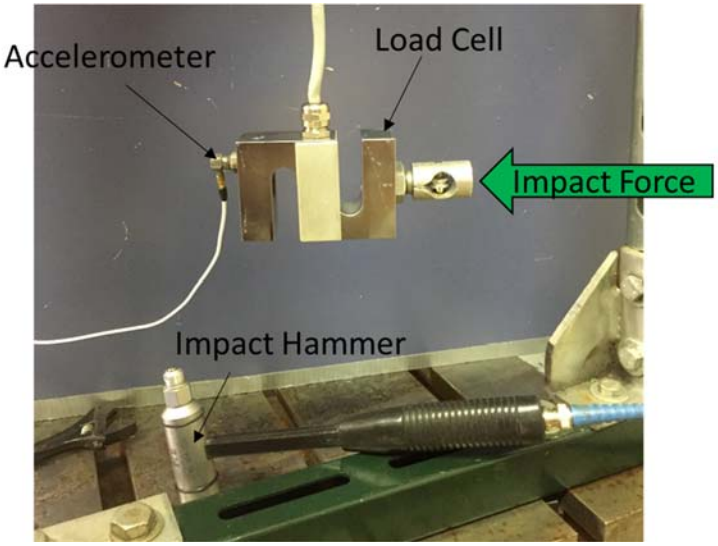

Figure 10. Impact load test to determine resonant frequency of a strain gauge load cell.

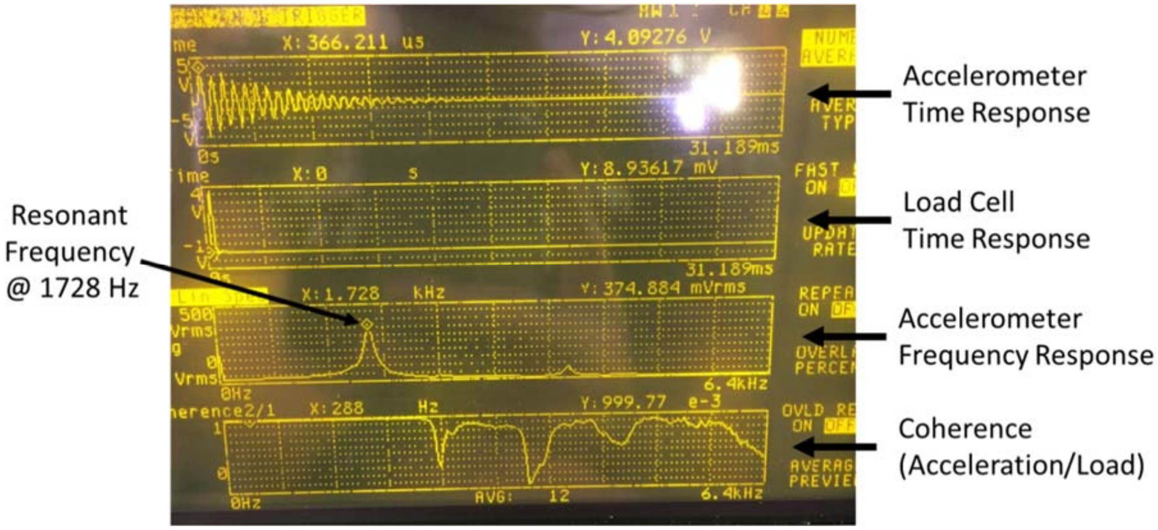

Figure 11. Dynamic signal analyzer output of strain gauge load cell impact test showing a resonant frequency at 1728 Hz with good coherence between the delivered impact load (input) and the measured acceleration (output).

Consequently, the loading mechanism is redesigned to better direct impact loads axially, to reduce resonant load cell interference, and to capture the test thrust bearing forced response. Figure 12 shows a diagram of the resulting taut cable system, and Figure 13 displays a photograph of the mechanism. A taut steel cable is routed through a hollow head impact tip to apply a static load to the system. One end of the impact tip is fastened rigidly to a load cell which is, in turn, threaded directly into the load shaft, while a flat surface on the opposite end receives impulse loads from an impact gun, as shown in Figure 14. The static load magnitude is controlled by adjusting the cable tension, while the magnitude of the impact load is configured through the impact hammer settings. The direction of the resultant load is manipulated by positioning the fixed ends of the cable using a pair of adjustable brackets. The result is a superimposed static and dynamic load oriented along just the axial direction, as desired. The dynamic load is measured with a load cell fastened between the impact tip and the load shaft. This load cell has an initial pre-load during installation so as to measure both compressive and tensile loads. The static load is derived using the system geometry, shown in Figure 12, and the cable tension, measured using a strain gauge load cell. The braided steel cable is 1.5 mm in diameter, and its stiffness is 93.15 ± 0.29 kN/m (see Appendix D for its estimation). By relocating the strain gauge load cell away from the axial load path, the resonant structural vibration of the instrument is no longer excited by the impact and, therefore, no longer interferes with the test thrust bearing response measurement.

Figure 15 shows measured accelerations from an axially mounted sensor on the TTB housing with (a) the previous configuration and (b) the new loading mechanism.

Increasing the structural stiffness of the loading mechanism reveals an overdamped system, as shown in Figure 15(b). Note that a third load cell, mounted at the tip of the impact hammer, triggers the data acquisition system.

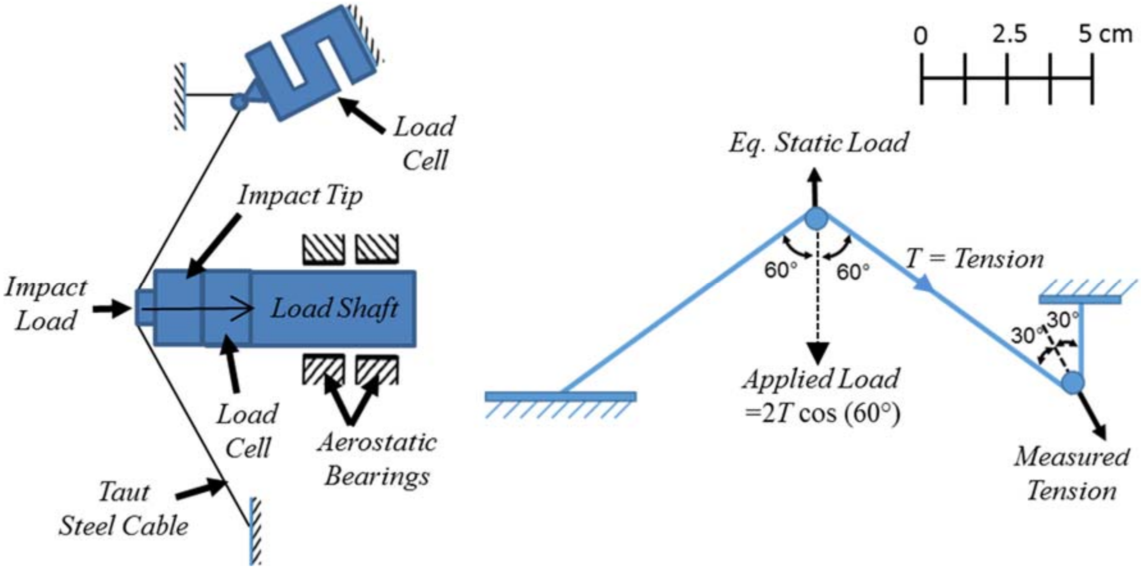

Figure 12. Schematic of redesigned, cable-loaded loading system and the geometry of the taut cable used to derive the equivalent static load along the axial direction, F_r.

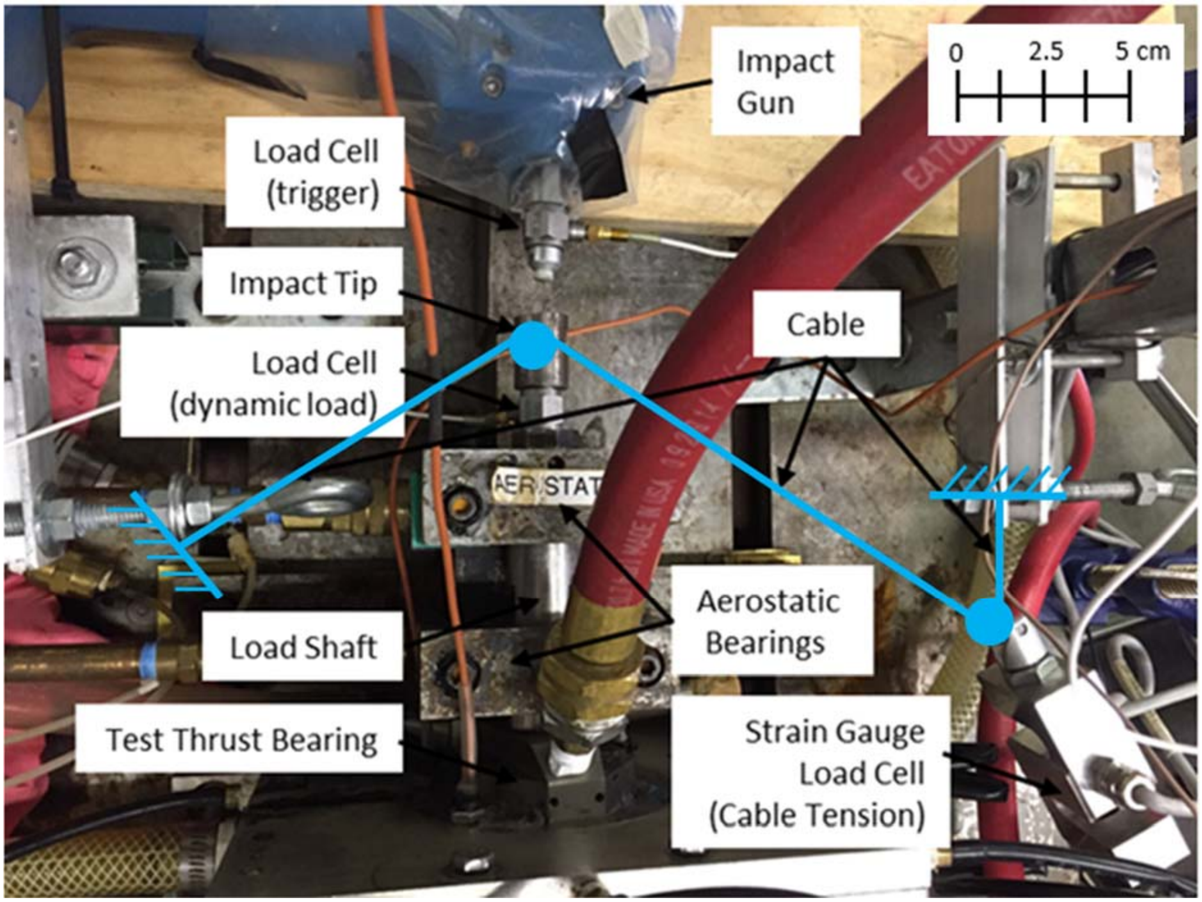

Figure 13. Photograph of taut cable load mechanism.

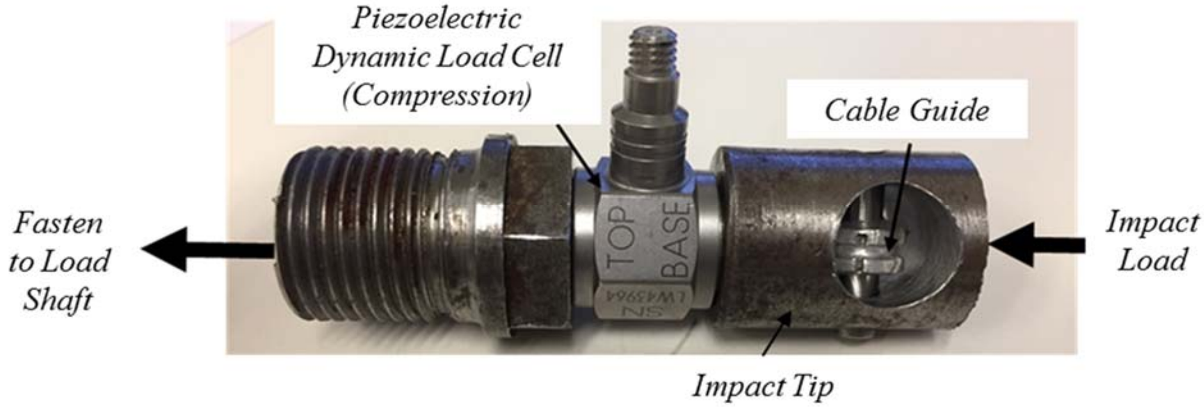

Figure 14. Photograph of the updated impact tip/load cell assembly. The dynamic load cell utilizes a threaded connection to both the impact tip and the load shaft. Preload is set by tensioning these threaded connections, enabling the dynamic load cell to measure both compressive and tensile forces.

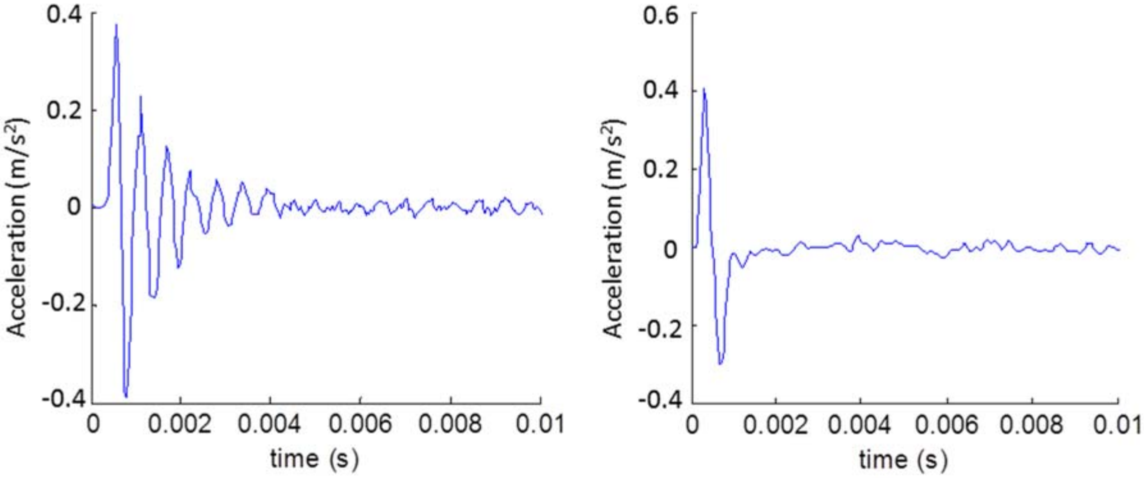

(a) Prior configuration

(b) Current configuration with taut cable

Figure 15. Axial acceleration measurements on TTB housing due to an impact load (a) with early configuration of load mechanism, and (b) with new configuration with taut cable.

SYSTEM MODEL FOR PARAMETER IDENTIFICATION

Thrust bearing force coefficients (stiffness K_{TTB}, damping C_{TTB}, and added mass M_{TTB}) enable the prediction and control of axial rotor motions under dynamic loading. Obtaining reliable estimates of the bearing operating performance in actual test conditions is (although challenging) necessary to validate predictive models [18].

Figure 16 shows a schematic view of the test thrust bearing and load shaft assembly modeled as a one degree of freedom (1-DOF) system[1]. Let z_{TTB} and z_R be the absolute axial displacements of the TB and rotor, respectively, and $z=z_{TTB}-z_R$ is the relative displacement between both components. Additionally, a taut steel cable with stiffness K_{Cable} applies the static force to the load shaft. A simple load vs. displacement experiment determines K_{Cable} as detailed in Appendix D. In Figure 16, a linear viscous damper (C_{TTB}), stiffness (K_{TTB}), and mass (M_{TTB}) coefficients denote the reaction of the thrust fluid film bearing.

---

[1] Model assumes no dynamic tilts or rotation, aligned rotor thrust collar and TTB face.

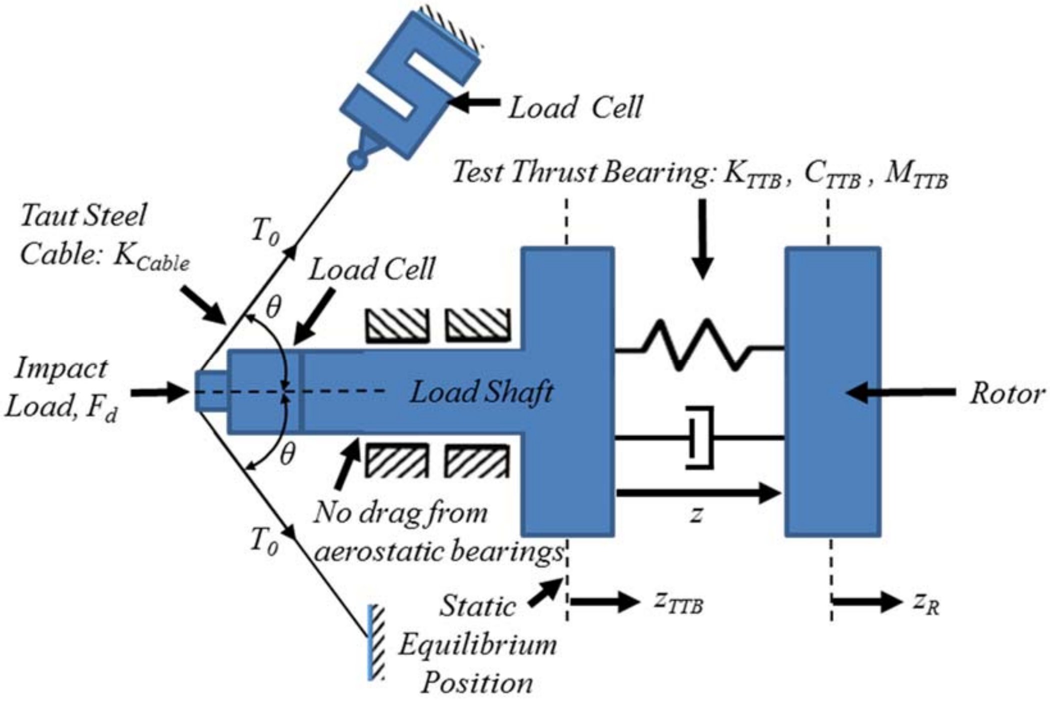

Figure 16. Schematic view of 1-DOF model of test TB for parameter identification.

The instrumentation used during the dynamic load tests includes six eddy current sensors (three on each thrust bearing), one piezoelectric accelerometer affixed to the test thrust bearing cartridge along the axial direction, and one load cell mounted on one end of the static loader. Three eddy current sensors define a plane and enable determination of the operating clearance at the center (C_0) of both the test TB and slave TB, as well as the tilt angles, if any.

At a static equilibrium, the applied load T_0 (from the taut cable) is balanced by the test TB force, ${F_{TB}}_0$, generated by an equilibrium clearance $C_0 = z_o$. Due to an impact load, $F_{d(t)}$, the test element (thrust bearing) in Figure 16 undergoes small amplitude motions about its static equilibrium position. The test and slave thrust bearings react to the dynamic force. Eddy current sensors record the ensuing motion while an accelerometer affixed to the load shaft assembly measures its acceleration ($\ddot{z}_{TTB}$).

Assuming no axial drag from the aerostatic bearings, the equation of motion (EOM) for the system undergoing axial motions is:

$$M\ \ddot{z}_{TTB} = F_{d(t)} + F_{Cable} - F_{TTB} \tag{1}$$

where M = 2.538 kg is the mass of the load shaft, TB and load cell, $F_{d(t)}$ is an applied impact load, F_{Cable} is the axial force applied by the taut cable on the load shaft (2Tcos60°), and F_{TTB} is the TTB reaction force equal to $F_{TTB} = F_{TTB_0} + F_{TTB_d(t)}$. Z_{TTB} represents TTB axial displacement and Z_R represents the axial displacement of the rotor as shown in Figure 16.

Assuming a massless and undamped cable, the force exerted by the cable is:

$$F_{Cable} = T_0 - K_{Cable}\ z_{TTB} \tag{2}$$

Where K_{cable} is the axial stiffness of the cable loading system. Appendix D describes the experimental apparatus to determine this stiffness.

At equilibrium,

$$F_{TTB_0} = T_0 \tag{3}$$

Represent the dynamic component of the TTB force as

$$F_{TTB_d(t)} \approx K_{TTB}\ z_{(t)} + C_{TTB}\ \dot{z}_{(t)} + M_{TTB}\ \ddot{z}_{(t)} \tag{4}$$

where K_{TTB}, C_{TTB}, and M_{TTB} are the bearing axial force coefficients (stiffness, damping and added mass, respectively). Hence, Eq. (1) becomes

$$M\,\ddot{z}_{TTB} = F_{d(t)} - K_{Cable}\,z_{TTB} - K_{TTB}\,z_{(t)} - C_{TTB}\,\dot{z}_{(t)} - M_{TTB}\,\ddot{z}_{(t)} \tag{5}$$

The discrete Fourier transform (DFT) algorithm transforms force, displacement and acceleration data from the time domain into the frequency domain [11]. Let

$$\overline{z}_{(\omega)} = DFT\left(z_{(t)}\right), \overline{F}_{(\omega)} = DFT\left(F_{(t)}\right), \overline{A}_{(\omega)} = DFT\left(\ddot{z}_{TTB_{(t)}}\right), \overline{z}_{TTB(\omega)} = DFT\left(z_{TTB_{(t)}}\right) \tag{6}$$

where ω denotes frequency. Recall that

$$i\omega\overline{z}_{(\omega)} = DFT\left(\dot{z}_{(t)}\right);\ -\omega^2\overline{z}_{(\omega)} = DFT\left(\ddot{z}_{(t)}\right) \tag{7}$$

where $i = \sqrt{-1}$ is the imaginary unit. Hence, in the frequency domain Eq. (5) becomes

$$H_{(\omega)} = \frac{\overline{F}_{d(\omega)} + \left(K_{Cable}/\omega^2 - M\right)\overline{A}_{(\omega)}}{\overline{z}_{(\omega)}} = K_{TTB} - M_{TTB}\omega^2 + i\omega C_{TTB} \tag{8}$$

Where H is the complex dynamic stiffness for the test element. With $H_{(\omega)}$ obtained, the estimation of the TB axial force coefficients follows from curve fitting of the real and imaginary parts of the complex dynamic stiffness, i.e.

$$Re\left(H_{(\omega)}\right) \rightarrow \left(K - M\,\omega^2\right)_{TTB}, Im\left(H_{(\omega)}\right) \rightarrow C_{TTB}\omega \tag{9}$$

DATA ACQUISITION AND PROCESSING

Data Acquisition

Two visual interface (VI) programs are written for impact load testing. The first VI uses to control the automatic impact hammer, through an analog voltage output module. The system is capable of delivering a specified number of impulse loads at a defined time interval. Typically, impacts are delivered on 5 second intervals to allow ample time for the system to settle back into an equilibrium axial position after excitation.

Figure 17 shows the second VI used to record impact test data. A load cell mounted on the tip of the automatic impact hammer is used as a trigger to begin data acquisition. Triggering parameters are configured directly from the VI. Once the trigger signal surpasses the specified level, the program records data, including a defined number of pre-trigger samples (a standard 10 pre-trigger samples are taken for all test conducted herein). The number of samples taken per test and the sampling frequency are also configured on the VI. For the subsequent Fast Fourier Transform (FFT) analysis, the number of data points must be a power of two; however, an additional two samples are needed to differentiate the recorded displacement signal for comparison with the recorded acceleration signal which drives the selection of $2^{14}+2 = 16{,}386$ samples/test. With this sampling rate and the number of instruments used, the maximum sampling rate for the data acquisition chassis is used, 31,250 Hz, yielding 0.52 seconds of recorded data for each test. The graph towards the top of the VI shown in Figure 17 reveals raw data from each test and is used for quick, real-time data quality assurance.

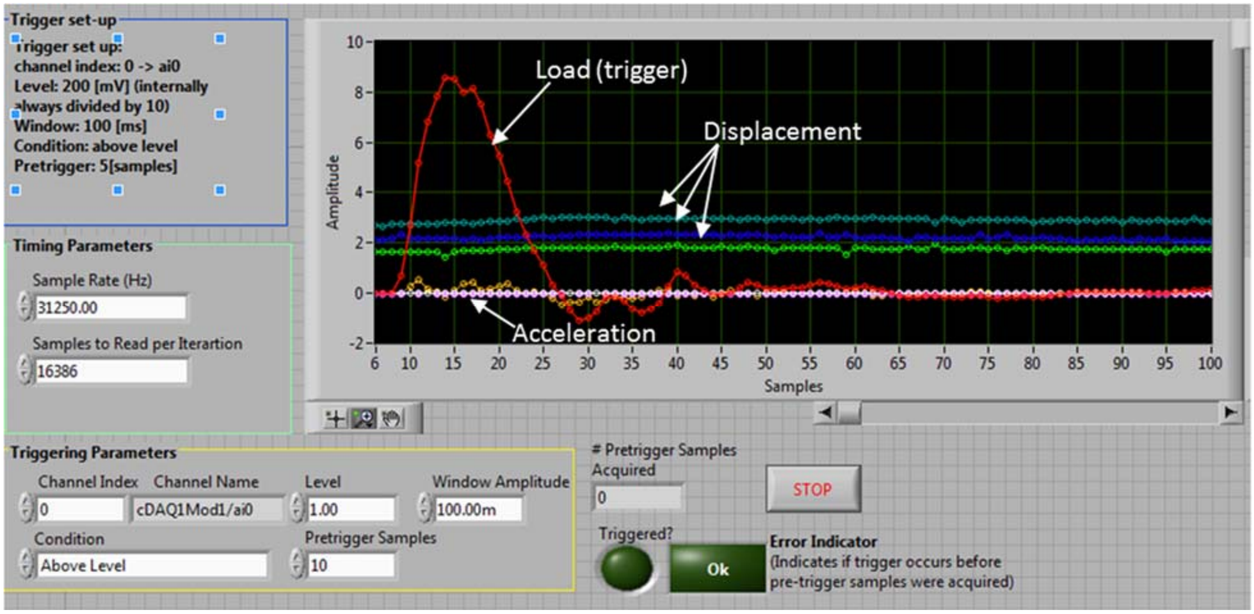

Trigger set-up

Trigger set up:
channel index: 0 -> ai0
Level: 200 [mV] (internally always divided by 10)
Window: 100 [ms]
Condition: above level
Pretrigger: 5[samples]

Timing Parameters

Sample Rate (Hz): 31250.00

Samples to Read per Iterartion: 16386

Triggering Parameters

Channel Index: 0

Channel Name: cDAQ1Mod1/ai0

Level: 1.00

Window Amplitude: 100.00m

Condition: Above Level

Pretrigger Samples: 10

Pretrigger Samples Acquired: 0

Error Indicator
(Indicates if trigger occurs before pre-trigger samples were acquired)

Figure 17. Visual Interface (VI) front panel recording dynamic impact test data.

The coherence between the load shaft acceleration and the impact load is monitored in real-time. A sound frequency identification range is determined for the region of coherence, *S*~1. Coherence results are remarkably consistent for frequencies between 0 and 250 Hz for each impact load.

Data Processing

A computational script processes the data recorded by the data acquisition system. Test parameters including number of impacts, frequency identification range, number of samples and sampling rate are user-defined. For each test examined herein, 100 impacts are averaged, each with 16,386 samples recorded at a rate of 31,250 Hz. The frequency identification range is determined in real-time between dynamic load and acceleration measurements taken with a dynamic signal analyzer.

The clearance (C_0) at the center of the TTB is calculated from axial displacements obtained from three eddy current proximity sensors installed on the TTB housing. Appendix B details the derivation of the TTB center clearance based on the three eddy current probe measurements and their fixed angular positions on the TTB face.

The frequency domain data provides the complex dynamic stiffness, $H(\omega)$. Real and imaginary parts of $H(\omega)$ are separated and then averaged for each test condition. Figure 18 shows an example of a linear curve fit for the average real and imaginary parts of $H(\omega)$ from 100 impacts. The axial force coefficients are determined using Eqn. (9).

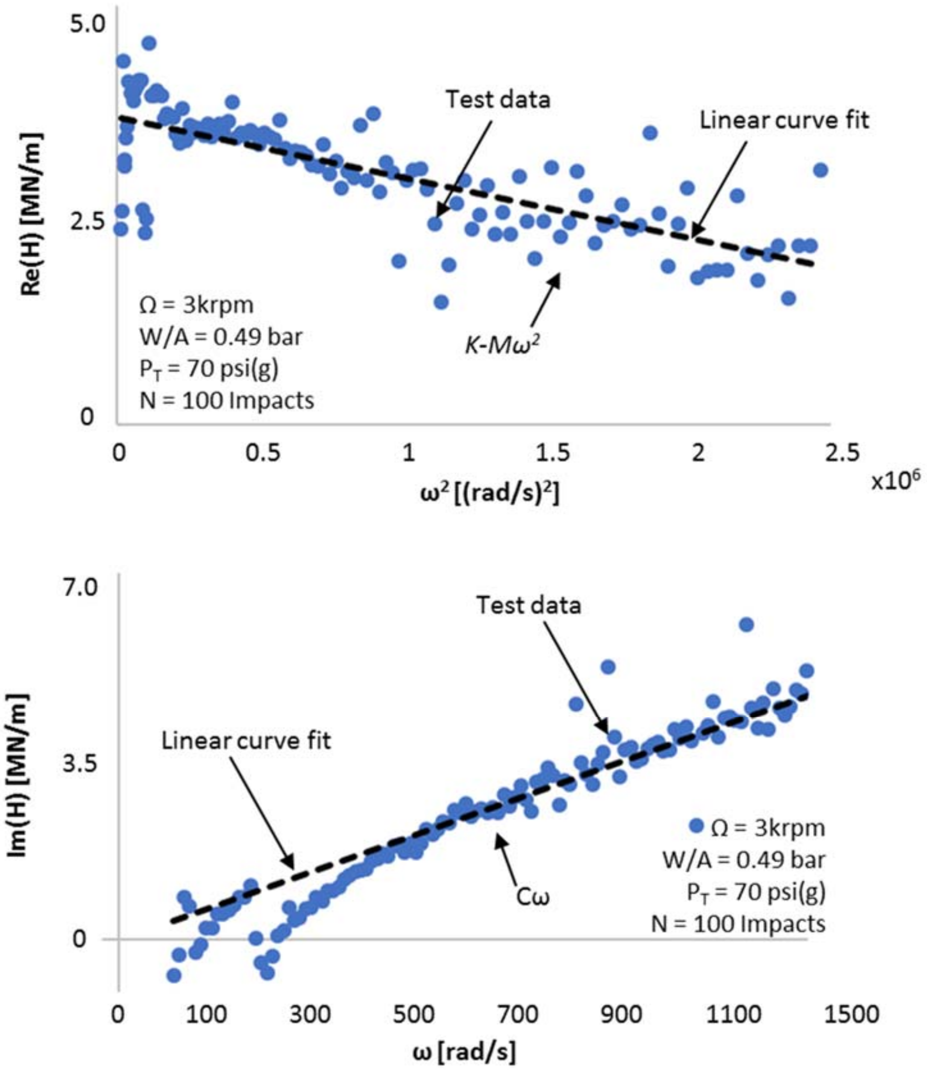

Figure 18. Sample linear curve fit of the (a) real and (b) imaginary portions of the TTB complex stiffness (*H*) vs frequency. *W/A* is the specific load defined as the axial load per unit area. Note that A = 32.6 cm^2.

THRUST BEARING PERFORMANCE

A series of tests are used to quantify the static and dynamic load performance of the test TTB for rotor speeds up to 6 krpm (ΩR_{out}=23.9 m/s). The next sections will outline both static and dynamic load test matrices as well as the results. Static load tests examine the effect of TTB supply pressure, applied axial load and shaft speed on the TTB axial clearance. Dynamic load tests examine the effect of these variables on the TTB bearing force coefficients, namely stiffness, damping and added mass. For all test conditions, water at a pressure of 3.45 bar(g) lubricates the radial bearings.

STATIC LOAD PERFORMANCE

Static load measurements are followed immediately by dynamic load tests. This is done to maximize repeatability of impacts during dynamic testing. This method necessitates the test rig instrumentation to be configured for dynamic load testing. Therefore, static load test results are limited to data acquired by the high speed data acquisition system used for dynamic testing, namely applied axial load and thrust bearing axial clearance.

At a null rotor speed, water supplies the axial test and slave thrust bearings with an increasing inlet pressure. Static load is then applied to the test thrust bearing using the cable tension loading system causing the bearing to load the rotor thrust collar. The specific static load, i.e., load per unit area (W/A) is used as a load metric. Note $A = 32.6$ cm^2 = $\frac{1}{4}\,\pi\,(D_{out}^2\text{-}D_{in}^2)$. The slave thrust bearing reacts to the applied load, thereby controlling rotor position. Finally, the electric motor gradually spins the rotor-coupling system up to test speed. Test speeds up to 6 krpm are performed, corresponding to a maximum surface speed of 24 m/s on the edge of the rotor thrust collar (R_{out}=7.62 cm).

The TTB supply pressure is measured using a pressure transducer positioned just upstream of the thrust bearing. With the supply pressure held constant, the static load system applies a decreasing load to the test thrust bearing. A decreasing load is applied to ensure that the lowest clearance (highest load) condition enables the rotor to spin freely at the onset of testing to avoid risk of contact between the rotor and TTB for subsequent load conditions. If the rotor does not spin freely the load shaft and TTB assembly must be aligned to the rotor thrust collar. After the conclusion of a static load condition, the motor stops, and the process repeats for the remaining supply pressure conditions.

Static Load Tests at Various Supply Pressures and Rotor Speeds

Table 1 outlines the static load test matrix designed to quantify the effects of distinct supply pressures and rotor speeds on the TTB static load performance at various applied load conditions. Figure 19 through Figure 22 present axial clearance vs. axial specific load (*W/A*) for rotor speeds ranging from 3krpm to 6krpm, respectively. The curves represent operation at TTB supply pressure of 2.76 bar(g), 3.45 bar(g), 4.14 bar(g) and 4.83 bar(g). Horizontal error bars represent uncertainty of the applied axial load while the vertical error bars represent the uncertainty of the calculated axial clearance at the center of the TTB. The large uncertainty[2] shown in Figures 21 through 28 are due to the allowable runout of each thrust collar (±10 µm). Appendix C presents a description of the uncertainty analysis is presented.

Table 1. Test Matrix for static load tests at null to moderate shaft speed.

Shaft Speed (krpm)	TTB Supply Pressure (bar(g))	Specific Load (*W/A*) (bar)
0, 3, 4, 5, 6	2.75	0.2 – 1.6
	3.45	
	4.14	
	4.83	

Figure 19 includes a solid line representing a sample prediction [2] for the 2.76 bar(g), 3 krpm test condition. Predictions match qualitatively with measurement trends

---

[2] Uncertainty for the static load results indicated with error bars at each data point.

although being consistently higher than the corresponding test data, with average percent differences of 25% to 53% [3]. Prior work [3, 5] presents correlation between static load measurements and predictions.

At a constant rotational speed, the TTB center clearance (*C₀*) decreases as the applied specific load increases. The difference in operating axial clearance between conditions of *Ps* = 2.76 bar(g) and 4.83 bar(g) is higher at lower clearances (high axial loads). The load differential decreases as the axial clearance increases (decreasing axial load). The behavior is consistent for each rotor speed and applied load condition indicating that TTB supply pressure is the primary factor affecting its static load performance. Note the axial clearance increases with an increase in TTB supply pressure.

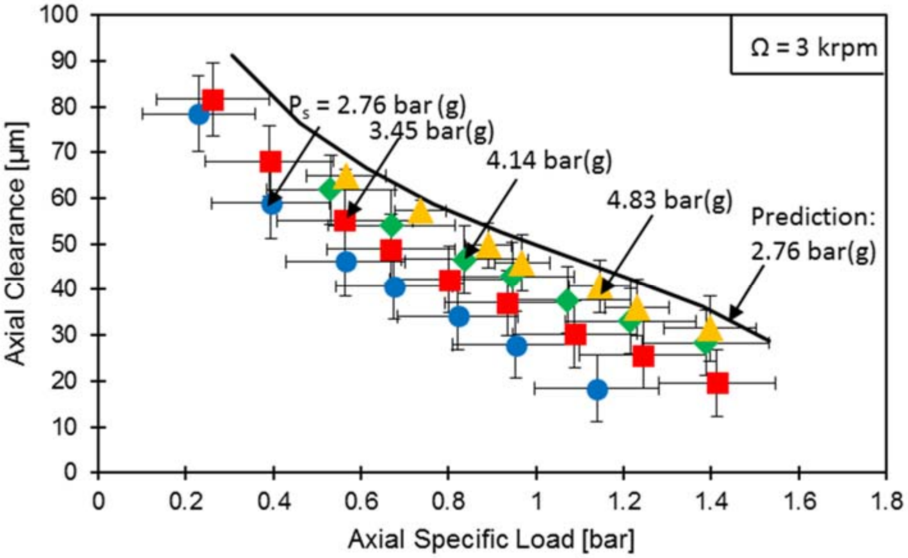

Figure 19. Axial clearance (*C_0*) versus specific load (*W/A*) for operation at four TTB supply pressures (P_s) and rotor speed at 3 krpm. Horizontal error bars represent the uncertainty in the axial load at a 95% confidence interval. Vertical error bars indicate the uncertainty in the axial clearance due to the machined runout of the rotor.

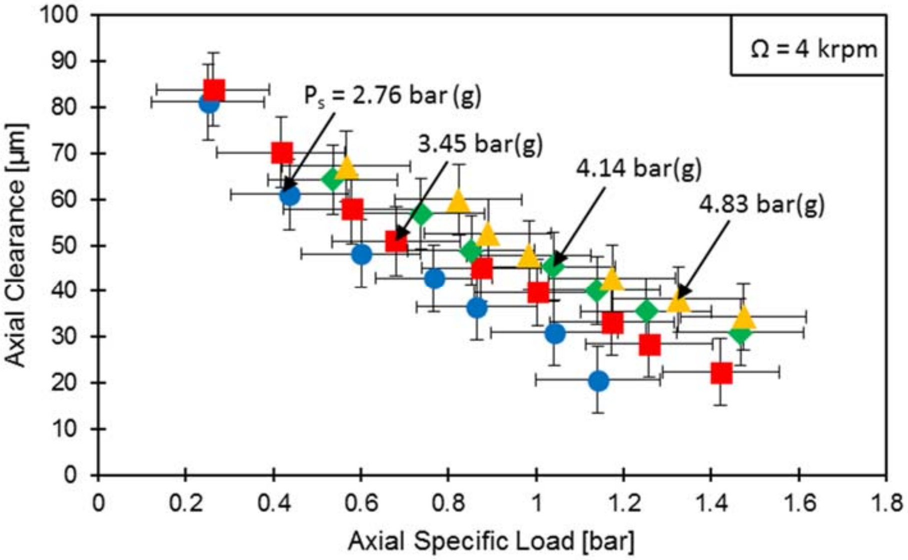

Figure 20. . Axial clearance (C_0) versus specific load (W/A) for operation at four TTB supply pressures (P_s) and rotor speed at 4 krpm. Horizontal error bars represent the uncertainty in the axial load at a 95% confidence interval. Vertical error bars indicate the uncertainty in the axial clearance due to the machined runout of the rotor.

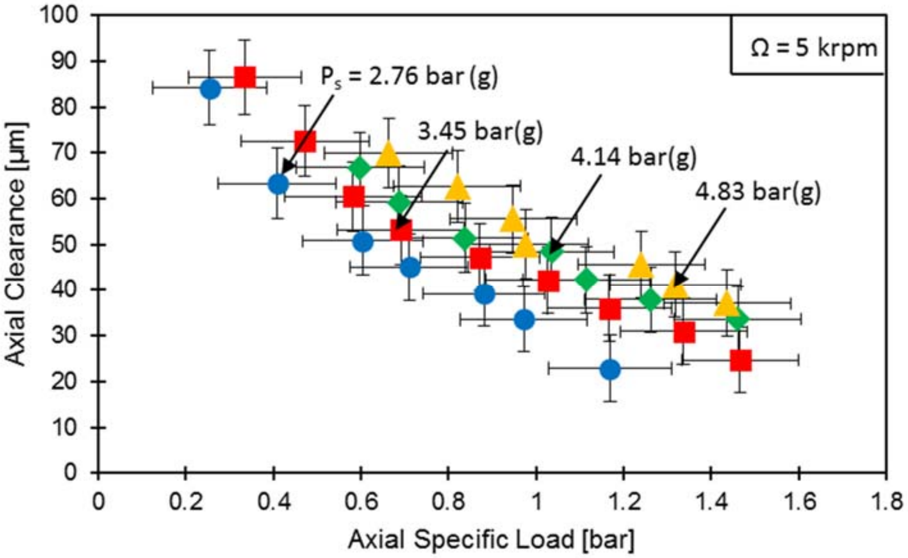

Figure 21. . Axial clearance (C_0) versus specific load (W/A) for operation at four TTB supply pressures (P_s) and rotor speed at 5 krpm. Horizontal error bars represent the uncertainty in the axial load at a 95% confidence interval. Vertical error bars indicate the uncertainty in the axial clearance due to the machined runout of the rotor.

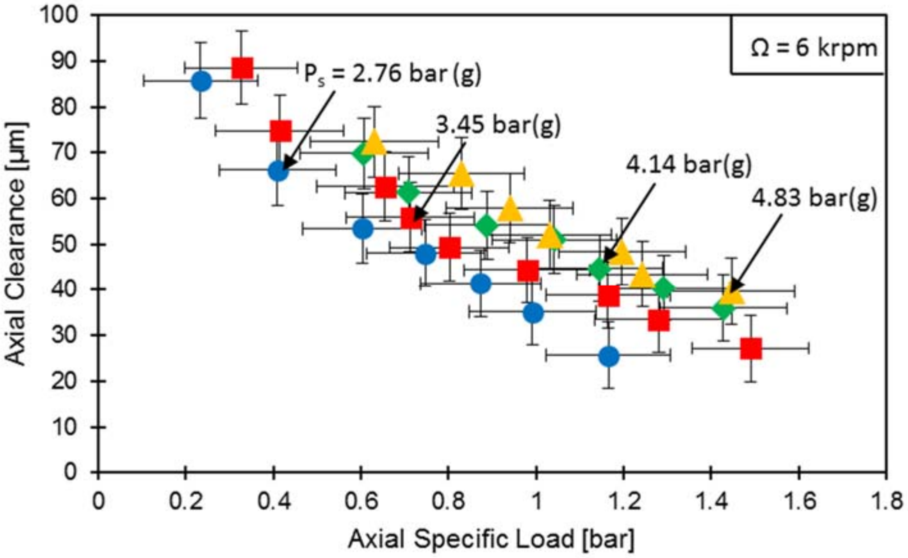

Figure 22. . Axial clearance (*C_0*) versus specific load (*W/A*) for operation at four TTB supply pressures (P_s) and rotor speed at 6 krpm. Horizontal error bars represent the uncertainty in the axial load at a 95% confidence interval. Vertical error bars indicate the uncertainty in the axial clearance due to the machined runout of the rotor.

Static Load Tests at Various Rotor Speeds

To quantify the effect of shaft speed on TTB static load performance, Figure 23 through Figure 26 show the axial clearance (C_0) vs. axial specific load for TTB supply pressures of 2.76 bar(g), 3.45 bar(g), 4.14 bar(g), and 4.83 bar(g), respectively. Rotor speeds of 0 krpm through 6 krpm are labeled on each graph.

At a constant TTB supply pressure (P_S), the axial clearance decreases marginally while the speed reduces from 6krpm to 3krpm. The axial clearance differential is larger at a lower axial clearance (higher load), indicating that the hydrodynamic component of the bearing reaction force is larger at small axial clearance. The null rotor speed condition represents pure hydrostatic operation.

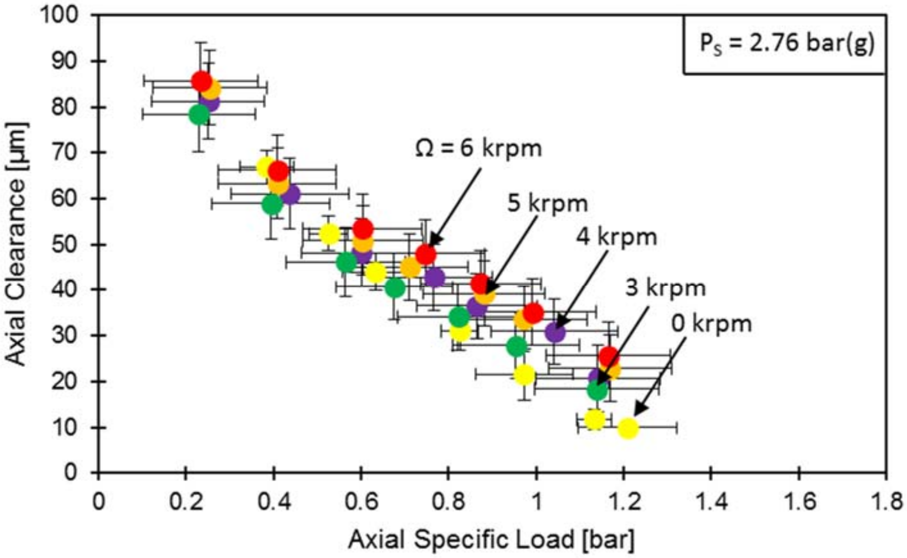

Figure 23. Axial clearance (*C_0*) versus specific load (*W/A*) for operation at various rotor speeds for operation with supply pressure *P_S* = 2.76 bar(g). Horizontal error bars represent the uncertainty in the axial load at a 95% confidence interval. Vertical error bars indicate the uncertainty in the axial clearance due to the machined runout of the rotor.

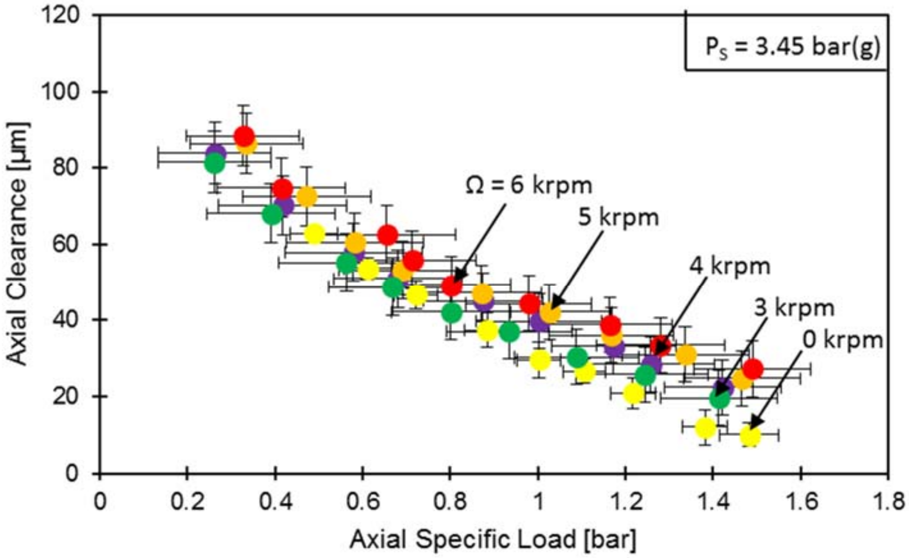

Figure 24. Axial clearance (*C_0*) versus specific load (*W/A*) for operation at various rotor speeds for operation with supply pressure *P_S* = 3.45 bar(g). Horizontal error bars represent the uncertainty in the axial load at a 95% confidence interval. Vertical error bars indicate the uncertainty in the axial clearance due to the machined runout of the rotor.

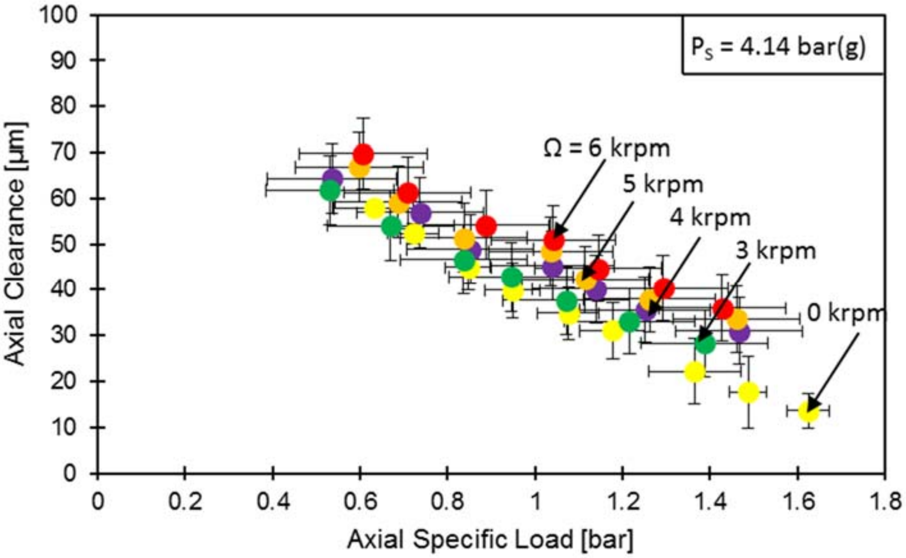

Figure 25. Axial clearance (*C_0*) versus specific load (*W/A*) for operation at various rotor speeds for operation with supply pressure *P_S* = 4.14 bar(g). Horizontal error bars represent the uncertainty in the axial load at a 95% confidence interval. Vertical error bars indicate the uncertainty in the axial clearance due to the machined runout of the rotor.

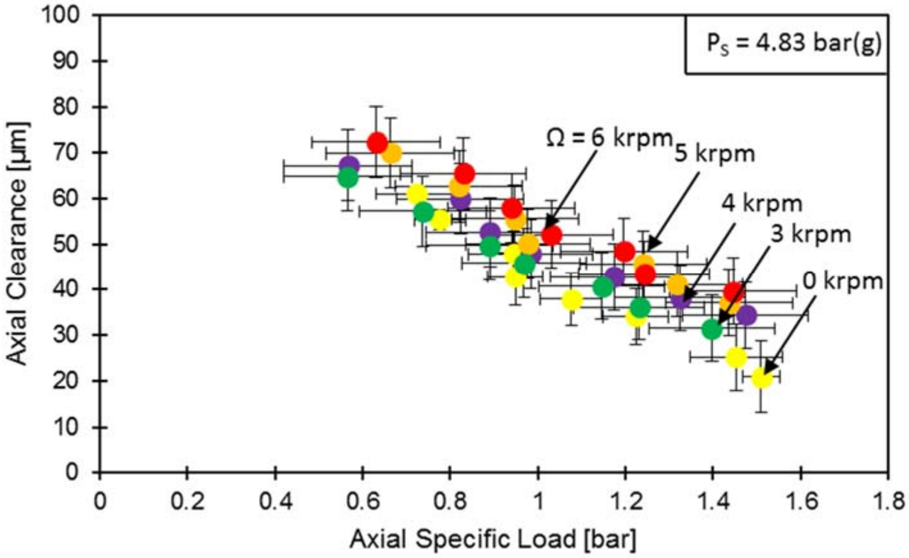

Figure 26. Axial clearance (*C_0*) versus specific load (*W/A*) for operation at various rotor speeds for operation with supply pressure *P_S* = 4.83 bar(g). Horizontal error bars represent the uncertainty in the axial load at a 95% confidence interval. Vertical error bars indicate the uncertainty in the axial clearance due to the machined runout of the rotor.

Static load results presented by Rohmer [15] match well with the current results for operation at null and 3 krpm rotor speed, and up to 4.14 bar(g) TTB supply pressure. Namely, the TTB axial clearance (C_0) increases as water supply pressure (P_s) increases under a constant applied load. The magnitude of said clearance is consistent with Rohmer's results [15], further verifying the performance of the test rig after extensive modification to the fluid supply system and axial loading mechanism.

DYNAMIC LOAD PERFORMANCE

Table 2 lists the test conditions used to assess the effect of TTB supply pressure and applied static load on the bearing force coefficients for operation at a constant rotor speed. Table 3 lists the test conditions used to analyze the dynamic effect of rotor speed while operating at a constant TTB supply pressure and applied static load. For variable rotor speed tests (up to 6krpm), the water supply pressure (P_s) is held at 4.83 bar(g) to ensure adequate load support.

Table 2. Test Matrix for dynamic load tests for operation at various TTB supply pressure and applied static load conditions.

Shaft Speed (Ω) [krpm]	TTB Supply Pressure (P_S) [bar(g)]	Specific Load (W/A) [bar]	Applied Load [N]	Equilibrium Clearance (C_0) [µm]
3	2.76	0.49	178	51.7 ± 7.7
		0.61	222	43.9 ± 7.3
		0.73	267	38.2 ± 7.2
	3.45	*Same as above*		60.6 ± 7.6
				52.3 ± 7.5
				45.7 ± 7.4
	4.13	*Same as above*		64.0 ± 7.7
				57.3 ± 7.7
				51.3 ± 7.6

Table 3. Test Matrix for dynamic load tests for operation at null to moderate shaft speeds.

Shaft Speed (krpm)	TTB Supply Pressure (bar)	Specific Load (bar)	Applied Load (N)	Equilibrium Clearance (C_0) (μm)
0	4.83	0.49	178	85.3 ± 1.1
		0.61	222	72.7 ± 1.3
		0.73	267	60.1 ± 1.5
3		*Same as above*		68.1 ± 7.6
				63.8 ± 7.7
				57.5 ± 7.7
4		*Same as above*		69.3 ± 7.6
				65.9 ± 7.7
				62.5 ± 7.7
5		*Same as above*		77.9 ±7.6
				72.4 ± 7.6
				66.8 ± 7.7
6		*Same as above*		77.2 ± 7.6
				73.1 ± 7.6
				68.9 ± 7.7

Dynamic Load Tests at Various Supply Pressures and a Fixed Rotor Speed

Prior to initiating motor speed, 3.45 bar(g) pressurized water flows into the radial bearings allowing the rotor to spin freely by hand. Water then supplies the axial test and slave thrust bearings with a constant pressure, P_s, as prescribed by Table 2. The cable tension loading system shown in Figure 12 applies the prescribed static load. The slave thrust bearing reacts to the applied load. The electric motor gradually spins the rotor-coupling system up to a speed of 3krpm. Upon meeting the test condition, a series of impact loads excite the load shaft and thrust bearing in the axial direction. Impact data sets are individually converted into the frequency domain and then averaged. The process repeats for supply pressures of 2.76, 3.45 and 4.13 bar(g).

Figure 27 shows the identified thrust bearing stiffness (K_z) vs. water supply pressure (P_s) and operation at 3 krpm shaft speed. With an increase in supply pressure, the axial stiffness increases. This behavior correlates well with the predicted stiffness [2] although the rate of increase is higher than that of the experimental magnitude. A change in applied axial load has minimal influence on K_z, indicating that P_s is the primary driver of stiffness K_z.

Error bars shown in the bearing coefficient results below indicate the measurement uncertainty associated with the dynamic load testing method. The large uncertainty is due in part to the allowable run out of the thrust collar (±10μm) and the repeatability uncertainty associated with the load impact tests as detailed in Appendix C. Repeatability uncertainty is low compared to the uncertainty of clearance measurements.

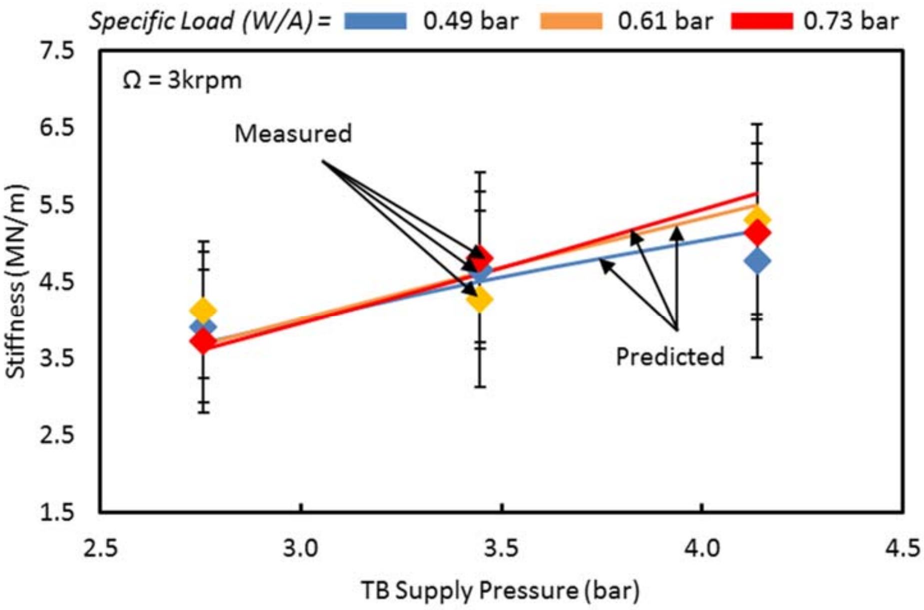

Figure 27. Experimentally measured and predicted axial stiffness coefficient (*Kz*) for TTB operating with water supplied at 2.75, 3.45 and 4.14 bar(g) and shaft speed of 3 krpm. Applied specific axial load, *W/A* = 0.49 bar, 0.61 bar, and 0.73 bar.

Figure 28 shows the axial damping (C_z) vs. water supply pressure (P_s) and operation at 3 krpm shaft speed. The graph shows data for three applied specific load conditions, *W/A* = 0.49, 0.61, and 0.73 bar. The predicted damping increases with an increase in supply pressure. The qualitative increase in measured damping agree with predictions although the magnitude of the measured damping values exceeds predictions for all but the P_s = 3.45 bar(g), *W/A* = 0.61 bar specific load test condition. A change in applied axial load has minimal influence on C_z, although for P_s = 2.76 bar(g) identified C_z coefficients decreases with increasing load. Similar to stiffness K_z, TB supply pressure P_s influences damping C_z more than applied load.

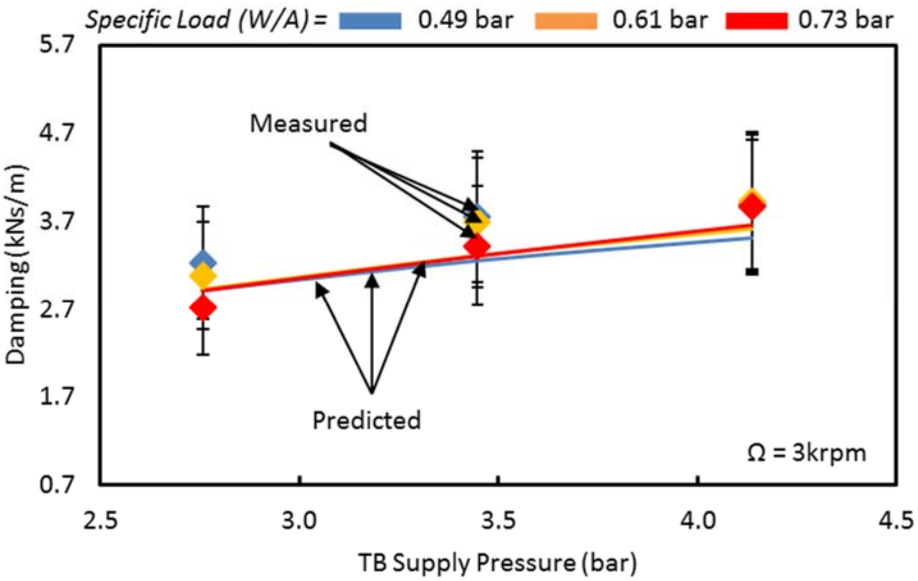

Figure 28. Measured and predicted damping coefficient (*Cz*) for TTB operating with water supplied at 2.75, 3.45 and 4.14 bar and shaft speed of 3 krpm. Applied specific axial load, *W/A* = 0.49 bar, 0.61 bar, and 0.73 bar.

Figure 29 shows the identified added mass (M_z) vs. water supply pressure and operation at a constant 3krpm shaft speed. The graph presents results for three applied specific load conditions, W/A = 0.49, 0.61, and 0.73 bar. The added mass coefficient exceeds the predicted magnitude for all cases (ranging from 8% to 32% difference). Both predictions and measurements indicate a minimal change in coefficient magnitude with an increase in water supply pressure. The maximum percent difference between the maximum and minimum supply pressures, P_s, is only 29% for the W/A = 0.73 bar applied load case.

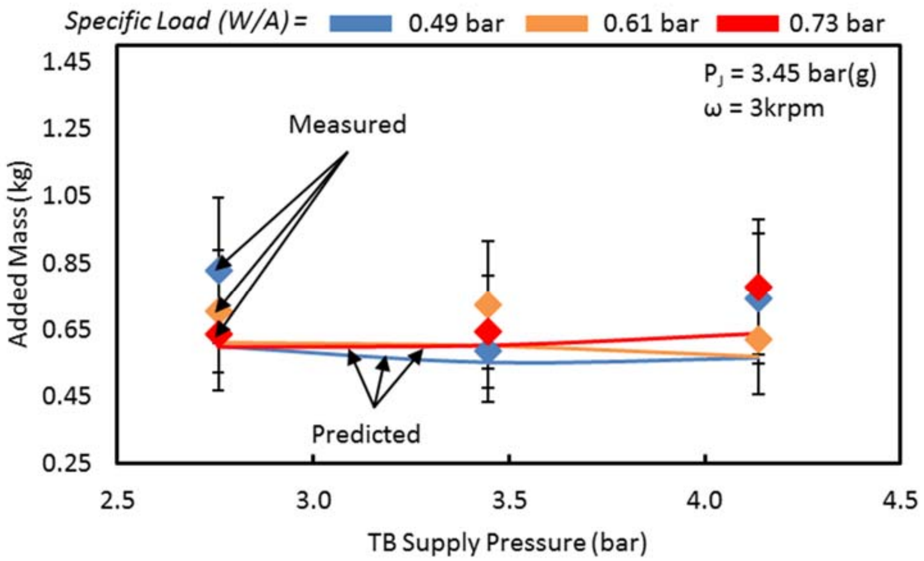

Figure 29. Measured and predicted added mass coefficient (*Mz*) for TTB operating with water supplied at 2.75, 3.44 and 4.13 bar and shaft rotational speed of 3 krpm. Applied specific axial loads of 0.49 bar, 0.61 bar, and 0.73 bar.

Dynamic Load Tests at Various Rotor Speeds and a Fixed Supply Pressure

3.45 bar(g) pressurized water flows into the radial bearings allowing the rotor to spin freely by hand before starting the electric motor. Water then supplies the axial test and slave thrust bearings with a constant pressure, P_s = 4.83 bar(g). The cable tension loading system shown in Figure 12 applies progressively decreasing TTB static load. The slave thrust bearing reacts to the applied load. The electric motor gradually spins the rotor-coupling system up to test speed. Upon meeting the prescribed dynamic load test condition, a series of impact loads excite the load shaft and thrust bearing in the axial direction. Impact data sets are individually converted into the frequency domain and then averaged. The process repeats for shaft speeds increasing from 3 krpm to 6 krpm as indicated in Table 3.

Figure 30 shows measured and predicted stiffness (K_z) vs. rotor speed for static loads, W/A = 0.49, 0.61 and 0.73 bar, with a constant 4.83 bar TTB supply pressure. As expected, as the static load increases, the bearing stiffness K_z also increases. As rotor speed increases, however, K_z does not change appreciably. Both measurements and predictions capture this behavior, this indicating the TTB performs primarily as a hydrostatic bearing.

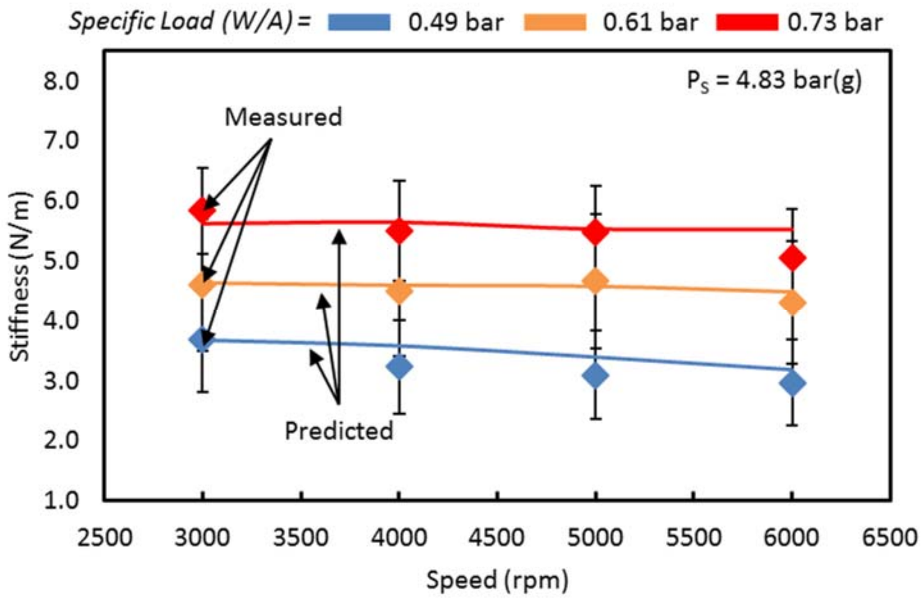

Figure 30. Measured and predicted stiffness (K_z) for the TTB operating with water supplied 4.83 bar and shaft speed of 3 krpm, 4krpm, 5krpm and 6krpm. Specific axial load *W/A* = 0.49 bar, 0.61 bar, and 0.73 bar is applied to the TTB.

Figure 31 shows measured and predicted damping (C_z) vs. increasing rotor speed for the test thrust bearing subjected to three applied static loads, *W/A* = 0.49, 0.61 and 0.73 bar, with 4.83 bar TTB supply. Both predictions and measured results indicate a minimal change in damping (C_z) with an increase in rotor speed, while C_z increases as the static load increases. Although the test damping magnitude exceeds the predicted values for *W/A* = 0.73 bar, the magnitudes of predictions and measurements agree well overall.

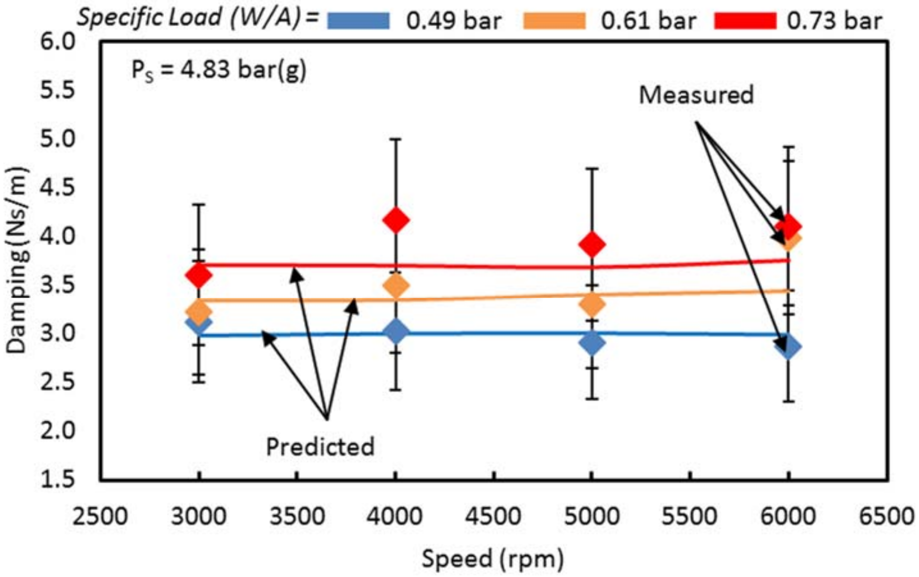

Figure 31. Measured and predicted damping (*C_z*) for the TTB operating with water supplied at 4.83 bar psi(g) and shaft speed of 3 krpm, 4krpm, 5krpm and 6krpm. Specific axial load *W/A* = 0.49 bar, 0.61 bar, and 0.73 bar is applied to the TTB.

Figure 32 shows the experimental added mass (M_z) vs. rotor speed for the TTB under three applied static loads, *W/A* = 0.49, 0.61 and 0.73 bar, with 4.83 bar TTB supply pressure. Predictions show no significant change in added mass with a change in shaft speed or applied load. The test results qualitatively agree with the prediction that M_z is minimally influenced by rotor speed. However, the magnitude of the test results exceed the predictions and indicate an increase in M_z with an increase in applied static load.

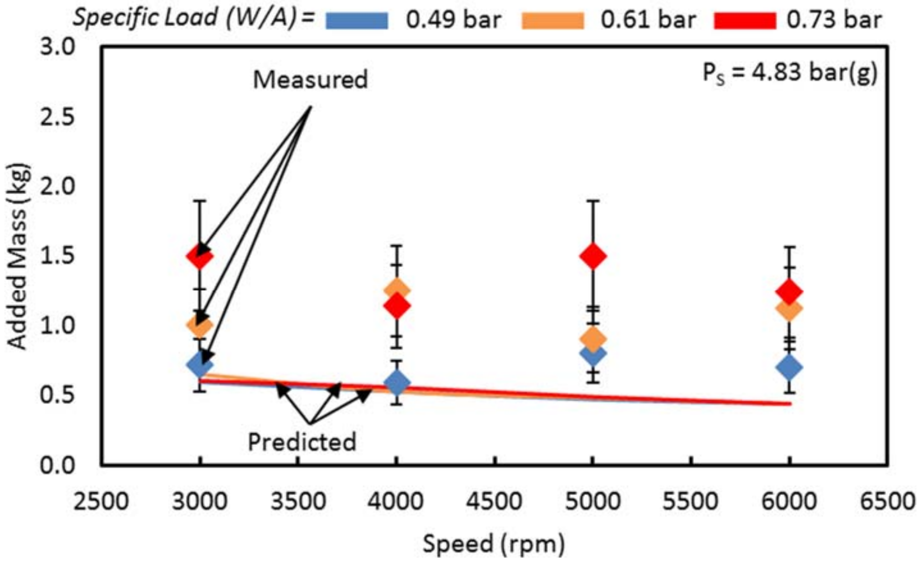

Figure 32. Measured and predicted added mass (*M_z*) for the TTB operating with water supplied at 4.83 bar psi(g) and shaft speed of 3 krpm, 4krpm, 5krpm and 6krpm. Specific axial load *W/A* = 0.49 bar, 0.61 bar, and 0.73 bar is applied to the TTB.

CONCLUSION

After a successful static load testing campaign in 2015 [16], the thrust bearing test rig was modified to conduct dynamic tests to determine bearing force coefficients (stiffness, damping and added mass). Reliable lubrication flow is provided by a new, continuous water supply system designed to run continuously for long periods of time as required for dynamic testing and with little waste. Additionally, an innovative loading system enables simultaneous application of static and dynamic loads via a taut cable and an automated impact hammer. Ultimately, these modifications allow for more controlled and repeatable test conditions which benefit acquisition of both static load and dynamic load test data. The experimental results validate model predictions and augment the bearing design process for future projects.

Prior to testing for bearing force coefficients, static load measurements are taken. These results further validate effectiveness of the test rig in determining static force vs. displacement performance and confirm that the rig is functioning properly after modification to accommodate the dynamic loading mechanism and new water supply system. The measured static load behavior match well with predictive software as well as prior experimental results. At a constant axial load, the axial clearance (C_0) increases as the TTB lubrication pressure (P_s) increases. With a constant supply pressure (P_s), however, the test TB axial clearance (C_0) decreases as the applied axial load (W/A) increases. Large uncertainties, inherent with the test rig, continue to plague axial displacement measurements.

For operation at a moderate shaft speed (up to 6krpm), dynamic behavior of a water lubricated thrust bearing is measured through impact load testing and quantified with force coefficients derived from the system complex dynamic stiffness function. Measurements indicate that the test thrust bearing shows no appreciable change in dynamic force coefficients (axial stiffness, damping and inertia) with a change in rotor speed. This behavior proves the bearing behaves in a mainly hydrostatic mode as it lacks hydrodynamic features on the bearing surface such as tapered sections or tilting pads. In short, the bearing behaves as a purely hydrostatic bearing for the range of rotor speeds examined herein. With an increase in applied static load, however, the test bearing stiffness and damping increase while added mass does not show appreciable change. The measured bearing dynamic behavior with increasing static load corresponds well with predicted values. Finally, with a constant applied load and low rotor speed (3krpm), an increase in TB supply pressure increases the stiffness and damping coefficients but does not bearing inertia.

Uncertainties associated with the axial clearance measurements are large for static and dynamic load tests. This uncertainty is largely due to the runout tolerance of the rotor thrust collar. To mitigate this uncertainty in future tests, a new rotor could be machined with tighter tolerances for this critical dimension.

REFERENCES

[1] Rohmer, M. and San Andrés, L., 2014, "Revamping a Thrust Bearing Test Rig," Annual Progress Report to the Turbomachinery Research Consortium, TRC-B&C-03-2014, Turbomachinery Laboratory, Texas A&M University, May.

[2] San Andrés, L., 2002, "Effects of Misalignment on Turbulent Flow Hybrid Thrust Bearings," ASME J. of Trib., **124**(1), pp. 212-219.

[3] Rohmer, M., San Andrés, L., and Wilkinson, S. 2018, "Static Load Performance of a Water-Lubricated Hydrostatic Bearing," *J. Eng. Gas Turbines Power*, **140**(6), pp. 062401-062401-10.

[4] San Andrés, L., Childs, D., and Phillips, S., 2016, "A Water Lubricated Hybrid Thrust Bearing: Measurements and Predictions of Static Load Performance," *J. Eng. Gas Turbines Power*, **139**(2), pp. 022506-022506-10.

[5] San Andrés, L., 2006, "Hybrid Flexure Pivot-Tilting Pad Gas Bearings: Analysis and Experimental Validation," ASME J. Tribol., **128**, pp. 551-558.

[6] Rowe, W., 1983, *Hydrostatic and Hybrid Bearing Design*, Textbook, Butterworths, London, England, pp. 1-20, 46-68.

[7] Nosaka, M. and Kato, T., 2013, *Cryogenic Tribology in High-Speed Bearings and Shaft Seals of Rocket Turbopumps,* Textbook, Dr. Jürgen Gegner (Ed.), DOI: 10.5772/55733.

[8] San Andrés, L., 2000, "Bulk-Flow Analysis of Hybrid Thrust Bearings for Process Fluid Applications," ASME J. of Trib., **122**(1), pp. 170-180.

[9] Safar, Z.S., 1983, "Centrifugal Effects in Misaligned Hydrostatic Thrust Bearings,"

ASME J. of Trib., **105**, pp. 621-624.

[10] Santiago, O., San Andrés, L., 2007, “Field Methods for Identification of Bearing Support Parameters- Part I: Identification from Transient Rotor Dynamic Response due to Impacts,” ASME J. Eng. Gas Turbines Power, **129**, pp. 205-212.

[11] San Andrés, L., 2010, “Modern Lubrication Theory, Experimental Identification of Bearing Force Coefficients,” Notes 14, Texas A&M University Digital Libraries, http://oaktrust.library.tamu.edu/handle/1969.1/93254 [5 April 2016].

[12] Forsberg, M., (2008), “Comparison Between Predictions and Experimental Measurements for an Eight Pocket Annular Hydrostatic Thrust Bearing,” Final Report, Texas A&M University, May-College Station, TX

[13] Ramirez, F., 2008, “Comparison between Predictions and Measurements of Performance Characteristics for an Eight Pocket Hybrid (Combination Hydrostatic/Hydrodynamic) Thrust Bearing,” M.S. Thesis, Mechanical Engineering, Texas A&M University, College Station, TX.

[14] Esser, P., 2010, “Measurements versus Predictions for a Hybrid (Hydrostatic plus Hydrodynamic) Thrust Bearing for a Range of Orifice Diameters,” M.S. Thesis, Mechanical Engineering, Texas A&M University, College Station, TX.

[15] Rohmer, M., 2015, “A Test Rig to Measure the Static Load Performance of a Water Lubricated Thrust Bearing,” M.S. Thesis, Mechanical Engineering, Texas A&M University, College Station, TX.

[16] Rohmer, M., Wilkinson, S. and San Andrés, L., 2015, "Revamping and Preliminary Operation of a Thrust Bearing Test Rig," Annual Progress Report to the Turbomachinery Research Consortium, TRC-B&C-03-2015, Turbomachinery Laboratory, Texas A&M University, College Station, TX.

[17] Rohmer, M., Wilkinson, S., Jani, H. and San Andrés, L., 2016, "Measurement of Static Load Performance in a Water Lubricated Hybrid Thrust Bearing," Annual Progress Report to the Turbomachinery Research Consortium, TRC-B&C-03-16, Texas A&M University, College Station, TX, May.

[18] Tiwari, R., Lees, A.W., Friswell, M.I. 2004, "Identification of Dynamic Bearing Parameters: A Review," Shock Vib. Dig., 36, pp. 99-124.

[19] Coleman, H. and Steel, W., 1989, "Experimentation and Uncertainty Analysis for Engineers," John Wiley and Sons, Inc., pp. 1-71.

APPENDIX A

INSTRUMENTATION

Table 4. Instrumentation utilized for TTB dynamic load testing

Name	Model/Serial Number	Sensitivity (Manufacturer)	Linearity (Manufacturer)
TT1 Proximity Sensor	SKF CMSS65-002-00-12-10 61112 11	7.87 mV/um	±5%
TT2 Proximity Sensor	SKF CMSS65-002-00-12-10 61112 12	7.87 mV/um	±5%
TT3 Proximity Sensor	SKF CMSS65-002-00-12-10 61112 01	7.87 mV/um	±5%
Accelerometer	PCB 353 B15/89602	9.81 mV/g	±10%
Strain Gauge Load Cell	Omega Engineering LC101-500/ 340069	16.71 mV/lbf	±0.03%
Dynamic Load Cell	PCB 208 M51/ 7192	14 mV/lbf	±15%

APPENDIX B

ROTOR THRUST COLLAR PLANE EQUATION DERIVATION

Thrust Collar Plane Equation

Forsberg [12] prepared the following original analysis. Eddy current sensors face a thrust collar and measure the axial gap between the thrust collar and TB surface at three circumferential locations, as shown in Figure 33. Using the gap clearances and the geometry to determine the clearance between the thrust collar and the TB surface at the center of the TB and the tilt of the thrust collar relative to the TB is critical in order to estimate the TB performance.

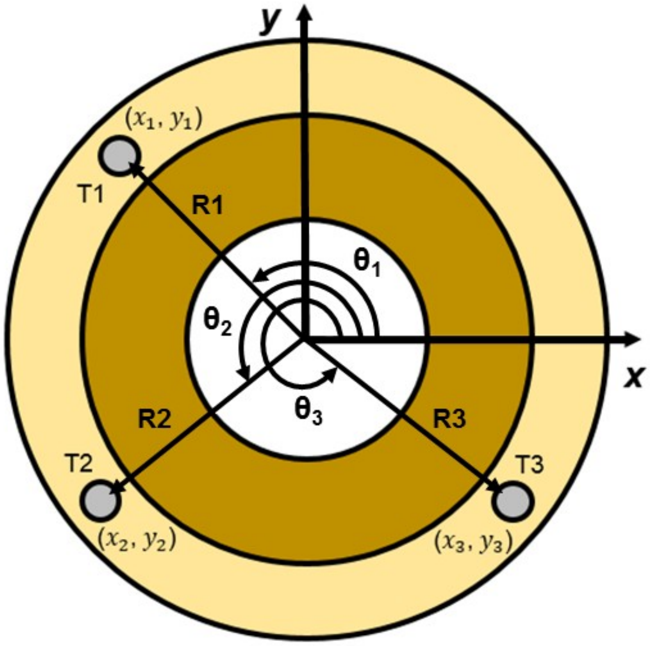

Figure 33: Reference diagram of a thrust bearing for geometric calculation of clearance as a function of displacements recorded at T1, T2, and T3.

Table 5 describes the horizontal and vertical positions of each eddy current sensor relative to the center of the TB.

Table 5. Horizontal and vertical positions of each eddy current sensor relative to the center of the thrust bearing.

	X	y
Probe T1	$x_1 = -33.02$ mm	$y_1 = 27.69$ mm
Probe T2	$x_2 = -37.34$ mm	$y_2 = -21.59$ mm
Probe T3	$x_3 = 37.34$ mm	$y_3 = -21.59$ mm

Assuming the TB and the thrust collar act as rigid planes, the gap between the thrust collar and the TB surface at each eddy current sensor can be used with the position of each eddy current sensor to determine the equation of the plane of the rotor thrust collar relative to the TB. To derive the rotor thrust collar plane equation, first establish a vector to define the distance from the TB center to each sensor and the angle between each vector and the x-axis as,

$$R_i = \sqrt{{y_i}^2 + {x_i}^2} \quad , \quad \theta_i = \tan^{-1}(y_i/x_i) \tag{C1}$$

respectively.

The axial gap at the center of the TB (C_0) as well as the tilt of the rotor thrust collar about the x-axis (δ_x) and y-axis (δ_y) relative to the TB define the clearance at any point on the thrust collar surface (C_i),

$$C_i = C_0 + R_i \cos\theta_i \,\delta_y + R_i \sin\theta_i \,\delta_x \tag{C2}$$

which can be simplified to the following form,

$$C_i = C_0 + X_{Si}\delta_y + \mathrm{Y}_{Si}\,\delta_x \tag{C3}$$

The transformation matrix,

$$A_T = \begin{bmatrix} 1 & X_{S1} & Y_{S1} \\ 1 & X_{S2} & Y_{S2} \\ 1 & X_{S3} & Y_{S3} \end{bmatrix} \tag{C4}$$

enables the conversion of the axial clearance measurements from each sensor (C_1, C_2, and C_3) into C_0, δ_y and δ_x with the following relation,

$$\begin{bmatrix} C_0 \\ \delta_y \\ \delta_x \end{bmatrix} = A_T \begin{bmatrix} C_1 \\ C_2 \\ C_3 \end{bmatrix}$$

APPENDIX C

UNCERTAINTY ANALYSIS

Static Load Measurements

Forsberg [12] and Rohmer [15] prepared the following original uncertainty analysis as it pertains to the thrust bearing test rig. The rotor thrust collars are fabricated with a run out tolerance of ±5 µm. This run out contributes to a ±5 µm uncertainty when defining the null clearance of each sensor as well as a ±5 µm uncertainty when measuring the clearance of each sensor which equates to a total bias uncertainty of ±10 µm for each eddy current sensor.

The Kline McClintock method [19] determines the bias uncertainty of the calculated thrust bearing center displacement (β_{C_0}) using the bias uncertainty of each eddy current sensor (β_{z_1}, β_{z_2}, β_{z_3}).

$$\beta_{C_0} = \sqrt{\left(\frac{\delta C_0}{\delta z_1}\beta_{z_1}\right)^2 + \left(\frac{\delta C_0}{\delta z_2}\beta_{z_2}\right)^2 + \left(\frac{\delta C_0}{\delta z_3}\beta_{z_3}\right)^2}$$

Precision uncertainty is determined at 95% confidence using standard deviation and the t-distribution table.

$$\xi = t_{\alpha=0.025,df=1000} * \sigma$$

Where

ξ = precision uncertainty of static load measurements based off of a 95% confidence level

σ = standard deviation

$t_{\alpha=0.025,df=1000}$= t-table factor for 1000 degrees of freedom at a 95% confidence level

The total uncertainty for static load testing is determined from the precision and bias uncertainties using the following equation,

$$\varepsilon_{stat} = \sqrt{\xi^2 + \beta^2}$$

Where

ε_{stat} = total uncertainty based off of a 95% confidence level for the static load tests

Dynamic Load Measurements

Dynamic load measurements have two primary sources of uncertainty. The first stems from the aforementioned displacement uncertainty due primarily to the maximum allowed run out of the thrust collar (±10μm). This static load uncertainty transcends into the dynamic load measurements as the displacement is used to calculate the complex stiffness term for each test condition. The second uncertainty source is the repeatability associated with the dynamic test procedure.

For each test condition, the thrust bearing response from 100 impacts is recorded and averaged. To determine the repeatability uncertainty, each test is separated into four series of 25 impacts. Figure 34 shows the average bearing displacement response for four data series with operation at thrust and journal supply pressures of 3.45 bar (g) and 3krpm shaft speed. For each series, the bearing coefficients are calculated and the standard deviation is obtained for the added mass, stiffness and damping values.

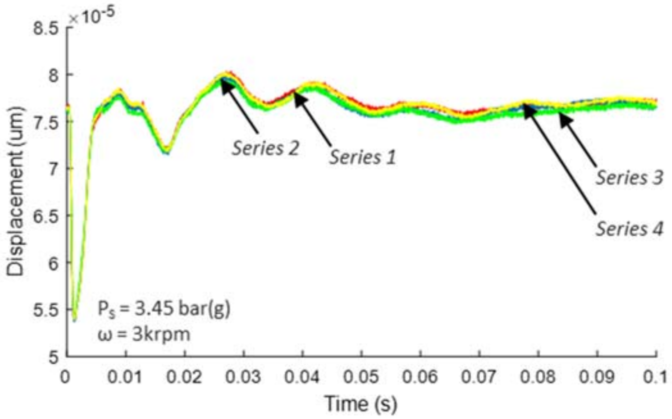

Figure 34. Averaged displacement response for four series of 25 impacts performed for operation at a rotor speed of 3krpm, thrust bearing supply pressure of 3.45 bar(g)

Precision uncertainty is determined at 95% confidence using standard deviation and the t-distribution table.

$$\xi_{dyn} = t_{\alpha=0.025,df=1000} * \sigma$$

where, ξ_{dyn} = precision uncertainty of static load measurements based off of a 95% confidence level

σ = standard deviation,

$t_{\alpha=0.025,df=1000}$= t-table factor for 1000 degrees of freedom at a 95% confidence level

The root sum square of the repeatability uncertainty and the static load testing uncertainty determine the bearing force coefficients for each test condition.

$$\varepsilon_{dyn} = \sqrt{{\varepsilon_{stat}}^2 + {\xi_{dyn}}^2}$$

Where

ε_{dyn} = total uncertainty based off of a 95% confidence level for the dynamic load tests

APPENDIX D

DETERMINATION OF CABLE STIFFNESS

Static Load is applied to the test thrust bearing using a taut steel cable oriented as shown in Figure 12. The stiffness of the steel cable in the TTB axial direction must be accounted for as it contributes to the total axial stiffness of the system. Axial stiffness of the static loading mechanism used for the dynamic load testing performed herein is determined experimentally.

Figure 35 illustrates the experimental setup used to determine the stiffness of the cable system. To replicate the geometry of the static loader used to determine bearing force coefficients, a steel cable is fixed at both ends on an optical table and subjected to a range of applied loads while monitoring displacement of the apex. The length of the un-stretched cable is identical to the length of the static loader cable. Load is administered using a small table-mounted winch and measured using a strain gauge load cell. Displacement of the apex is determined by marking the apex's position on the optical table for the various applied loads and measuring with a caliper gauge.

With the cable pulled taut, discrete loads are applied to the system with the winch as shown in Figure 35 and displacement of the apex is measured in the same direction. Applied force is plotted against the measured displacement in Figure 36. Assuming no plastic deformation, the experimental stiffness is the linear relationship between force and displacement. Using a linear fit on the experimental data presented in Figure 36, the stiffness of the cable loading system in the TTB axial direction is calculated to be 93.15 kN/m.

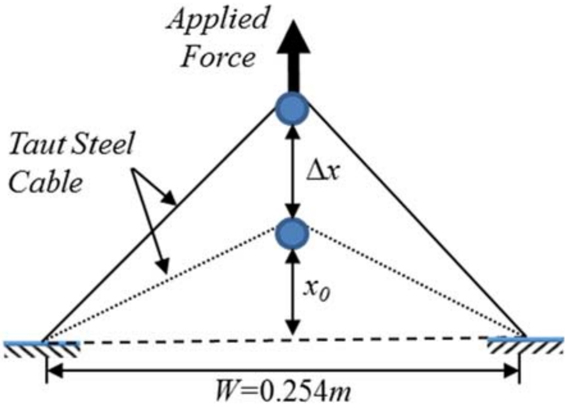

Figure 35. Schematic of an ad-hoc setup used to record the axial stiffness of a static loading mechanism.

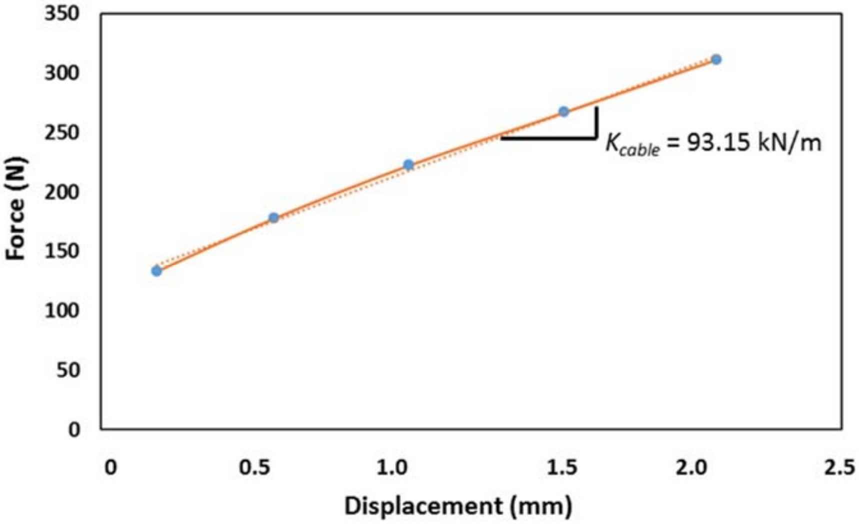

Figure 36. Applied force vs. displacement results for determination of the axial stiffness of the static loading mechanism.